Vascular Organization in the Primary Visual Cortex of the Macaque and Squirrel Monkey and its Relationship to Metabolic Activity

Dissertation

der Mathematisch-Naturwissenschaftlichen Fakultät

der Eberhard Karls Universität Tübingen

zur Erlangung des Grades eines

Doktors der Naturwissenschaften

(Dr. rer. nat.)

vorgelegt von

Anna Lena Keller

aus Stuttgart

Tübingen

2011

Tag der mündlichen Qualifikation:	07.10.2011
Dekan:	Prof. Dr. Wolfgang Rosenstiel
1. Berichterstatter:	Prof. Dr. Bruno Weber
2. Berichterstatter:	Prof. Dr. Andreas Nieder

Contents

Introduction

The primate brain can be characterized as the most complex, least understood and utmost demanding organ, and justifiably so. It consists of nearly 10^{11} neurons (Haug, 1986) connected via 10^{14} synapses (Braitenberg and Schüz, 1991), and the number of theoretically possible computational states of this network just exceeds any imagination. The numbers and possible functional influences of other cellular elements like the glial cells are not even considered in this. To date, the well-known search engine for biomedical literature PubMed (http://www.ncbi.nlm.nih.gov/pubmed) lists more than half a million articles published with the term "brain" in title or abstract, and it can be expected that this number will increase exponentially in the future. Compared to the whole organism, the brain is of relatively small size, but nevertheless it consumes about a quarter of the body's total glucose and a fifth of its oxygen (Nehlig, 1996). Taking into account that the brain lacks in actual storage capacity for energy substrates, one can assume high demands on the anatomical arrangement of the blood vessels and the spatiotemporal control of the energy supply.

Anatomy: Cortical Vascularization

In principle, the cortical vascular system seems to be organized similarly in most mammals (Bugge, 1985). Arterial blood is delivered to the head via the carotid and the vertebral arteries, which ramify to supply certain parts of the head and the brain with its branches. The large cephalic arteries run along the surface of the brain within the pial space and ramify further into smaller and smaller arteries that are connected among each other additionally by numerous anastomoses (Blinder et al., 2010). In the

end and at some points along their course they dive perpendicularly to the surface into the cortex, give rise to even smaller arteriolar vessels in different cortical depths which finally feed the capillary bed (Duvernoy et al., 1981). In these smallest elements of the vascular system, in the capillaries, most of the metabolically important exchange of oxygen and glucose between blood stream and brain tissue takes place. After a certain length the capillaries converge to venules, which lead into the perpendicular veins draining the cortex. These latter ones again conjoin with others on the cortical surface to larger and larger veins, ending in the several venous sinuses of the skull. From there, the blood is drained via the jugular and the vertebral veins (Butler, 1967). There is some variability across mammalian species, for example concerning the exact supply territories of the different large arterial and venous branches or the proportion to which these branches contribute to the overall maintenance of the brain's energy supply, but the general organization of the vascularization, especially within the cortex seems to follow the principles described above.

Physiology: Neurovascular Coupling

The tight relationship between neuronal activity, energy consumption and the following reaction of the vasculature, the so-called neurovascular coupling, is a topic that became of especially high interest just recently (Drake and Iadecola, 2007; Iadecola and Nedergaard, 2007; Jolivet et al., 2009; Tsai et al., 2009; Woolsey et al., 1996). As basis for the prospering non-invasive hemodynamic imaging techniques such as BOLD fMRI (blood oxygenation level dependent functional magnetic resonance imaging) the exact knowledge of all aspects that might play a role in neurovascular coupling is critical. The BOLD contrast generating the fMRI signal is influenced by multiple local occurrences following neural activation, such as the

consumption of oxygen and the subsequent increase in deoxyhemoglobin concentration, combined with an increase in blood flow and volume and a resulting net increase in oxygenated hemoglobin (Ogawa et al., 1990). Obviously, the changes in blood flow and volume underlie restrictions by the architecture of the vasculature, which therefore might have implications for the interpretation of the fMRI signal. The firm conviction about a strong interdependency of structure and function lead to the investigation of the anatomical organization and quantitative distribution of the brain's vasculature. Due to the relevance of the macaque monkey as a model organism in fMRI studies, this primate species was chosen as main subject of investigation, but the general organization principles seem to be very similar in most primates. The visual cortex is an intensely examined brain structure and well described in the literature. This is why we have chosen to analyze the cortical vascularization in this region of the monkey brain.

Metabolism: Cytochrome C Oxidase

The blood stream is the transport medium for glucose and oxygen and a relationship between the brain's vascularization and oxidative metabolism can be expected. Most of the brain's oxygen need is used for the oxidation of glucose to generate ATP (adenosine triphosphate), the universal carrier for energy exchange in all cells. In the last steps of this process, oxidative phosphorylation of ADP (adenosine diphosphate) to ATP occurs. These reactions are referred to as the respiratory chain and are located in the inner membrane of mitochondria. One of the enzymes involved in mitochondrial respiration is the cytochrome c oxidase (COX) whose activity can be visualized in histological sections of the brain up to several days after the death of an animal (Wong-Riley, 1979). The distribution of this enzyme and therefore presumably the degree of metabolic capacity is not constant over the whole brain, rather there

exist distinct patterns across layers and areas (Hevner et al., 1995; Ridge, 1967). The regional rate of oxidative enzymatic activity has been positively correlated to capillary density in rodents (Borowsky and Collins, 1989; Tuor et al., 1994) and primates (Zheng et al., 1991) already earlier. However, the results of the latter publication seemed questionable for which reason an extended replication of this study appeared appropriate (Keller et al., 2011). Zheng and colleagues investigated the vascularization of the so-called blobs in the primary visual cortex of squirrel monkeys, our replication comprised macaques as well. Anatomically the cytochrome oxidase blobs are characterized as zones of an increased activity of the oxidative metabolism, most prominently stainable in lower layer II/III of the primary visual cortex (Horton and Hubel, 1981) of several mammalian species, including all primates examined so far. Their exact function still remains elusive; however there is converging evidence that they are involved in the processing of color. As a matter of fact, what definitely distinguishes the blobs from their surround within the same layer is a direct projection from the lateral geniculate nucleus (LGN), the thalamic relay nucleus providing V1 with all visual information from the retina. However, one should keep in mind that this is not a peculiarity of the visual system alone, as all sensory information enters the cortex via the thalamus.

Functionality: Thalamocortical Projections

The spatial coincidence of increased COX activity with termination sites of thalamic inputs is a phenomenon that has already been noticed by several authors (Fitzpatrick et al., 1983; Livingstone and Hubel, 1982; Martin, 1988; Wong-Riley, 1979). Remarkable in this context is the usually rather low proportion of thalamocortical synapses. In the primary visual cortex of cats and macaques for example, thalamic afferents account for only about 5-10% of all synapses in direct thalamic projection

sites like for example layer IVc (Garey and Powell, 1971). It has been proposed that thalamocortical synapses are especially powerful (Gil et al., 1999) or that amplification through postsynaptic target neurons occurs (Stratford et al., 1996), whereas also evidence for the contrary can be found in the literature (Bruno and Sakmann, 2006). These authors state that the individual thalamocortical synapse is weak, but gains impact through highly synchronous activity, without the need for further amplification. What exactly causes the increased metabolic activity in these sites is still not clear, but the conclusion that it originates from the characteristic properties of the thalamocortical pathway suggests itself.

Relevance: Questions posed

Acute changes in blood flow following neuronal activity are restricted by the anatomy of the cortical vascularization. To enable a more reliable interpretation of the signals measured with hemodynamic imaging techniques a better knowledge about the vascular organization is essential. Especially when signals from different cortical regions are to be compared with each other, it is important to know if differences in vascular density exist which might bias the signals. Another relevant question concerning the functional interpretation of hemodynamic measurements with respect to the underlying mechanisms is to what part of the computational processes in an active region the signal correlates best, to the neuronal cell body or to the presynaptic side, to input or to output. This issue was approached by evaluating the covariation of the vascular density with the densities of neurons, synapses and glial cells, as well as with the net sum of oxidative metabolic activity. The latter relationship between vascularization and oxidative metabolism was investigated in greater detail to clarify if it correlates proportionally in general.

Summary of publications

#1: The Microvascular System of the Striate and Extrastriate Visual Cortex of the Macaque

In this first study, the general organization of the cortical vascularization in the macaque monkey brain was investigated and the quantitative differences of the vascular density across cortical layers and between visual areas were assessed. A variety of anatomical techniques was applied to achieve this.

Corrosion cast preparations were imaged with a scanning electron microscope to be able to qualitatively describe the microvascular organization and some of its anatomically peculiar characteristics. In general, the cerebral vascularization of the macaque was found to be organized very similarly to humans (Duvernoy et al., 1981). So-called plastic strips (Rodriguez-Baeza et al., 1998) could be found as well, around arteries, especially near the cortical surface and near branching points. In addition, it was possible to estimate the numerical ratio between large penetrating arteries and veins (Miodonski et al., 1976), which was found to be 1:~1.6 in favor of the arteries.

A fluorescent double staining approach was chosen to quantify the cortical vascular length density, surface area, volume fraction and vessel calibers. Immunohistochemical staining of blood vessels on the one hand (Fukuda et al., 2004) and staining of cell nuclei for structural orientation purposes on the other allowed for an exact region specific evaluation of the vasculature. These regions of interest were the different cortical layers (including white matter) in the visual areas V1, V2, V3, V4 and V5. The highest vascular length density was observed in the main input layer

of the visual cortex, namely layer IV of the extrastriate areas and layer IVc of striate cortex respectively. White matter always showed a considerably less dense vascularization, with an especially low capillary density, whereas vessels with larger diameters were more frequent. When the level of vascularization was compared across areas, primary visual area V1 reached the highest vascular density, being accompanied by a significantly smaller mean vessel diameter than in all other visual areas. This means that presumably it is mainly the capillaries that account for this surplus. The differences between the extrastriate areas were found to be negligible. To give an idea of the absolute values underlying this summarized report of the quantitative results, the mean vascular density in the gray matter of all examined visual areas corresponds to a volume fraction of 2.14% of the total tissue volume, with a range from 1.93% to 2.70% from the least to the most densely vascularized layer.

Moreover, as further histological method the cytochrome oxidase staining technique (Wong-Riley, 1979) was used to visualize the relative degree of local oxidative metabolism across cortical layers. The cytochrome oxidase activity closely followed the laminar profile of the vascular density and the correlation was striking especially for the measures of the capillary density. Correlation of the vascular density with own measures of the cell density from the fluorescent nuclei stain, as well as with data from the literature for neuronal, glial and synaptic density (O'Kusky and Colonnier, 1982) turned out to be only weak. This finding suggests that it is the net sum of the energy demand of all cortical elements together that drives the metabolic need of a certain region and influences the development of the local angioarchitecture.

#2: Vascularization of Cytochrome Oxidase-Rich Blobs in the Primary Visual Cortex of Squirrel and Macaque Monkeys

The second study tied in with one of the outcomes of the aforementioned publication #1, illuminating the interdependency of cytochrome oxidase activity and vascularization in more detail. The phenomenon of the blobs described for area V1 of several species was an ideal candidate for a comparative examination of this relationship. Two primate species namely squirrel and macaque monkeys were investigated.

On tangential sections through the lower part of cortical layer II/III of V1 double staining for cytochrome oxidase and blood vessels was performed. On basis of the COX stain the blobs were defined and within and out of these regions of interest the relative COX stain intensity and the absolute vascular length density were measured. Additionally the number, location and diameter of feeding arteries and draining veins running perpendicularly to the cortical surface and the tangential sectioning plane were evaluated.

The species showed slight differences in some of the properties under examination, but only in absolute quantities, the qualitative results were the same for both. Overall, the squirrel monkeys exhibited a higher vascular density and more perpendicular blood vessels, but with a smaller diameter than the macaque. The comparative measurements of blob and interblob regions within one animal yielded similar results in both primate species.

The comparison between blob and interblob regions revealed a higher vascular density within the blobs (approximately 4.5%) and a ratio of perpendicular vessels of 1:1.2 in favor of the interblob areas. These findings were of special interest in two

ways. First of all, apparently they correct an earlier study carried out in squirrel monkeys (Zheng et al., 1991). As a matter of fact, the discrepancies between these already published results and own preliminary results from the macaque in the range of one order of magnitude led to the inclusion of squirrel monkeys to our study in the first place. And secondly, the relation between the intensity of the COX stain and the vascular density was found to be comparable in blobs and interblobs as well as across cortical layers, despite being measured in sections of different orientation. This proportionality supports the idea of an on principle entity of COX activity and degree of vascularization.

Discussion

Besides the qualitative description of the vascular organization and the reliable quantification of the vascular density in the visual cortex of two primate species, the main and common finding of both publications is the tight correlation of local capillary density and cytochrome oxidase activity. Assumedly this relationship is neither restricted to visual areas, nor to primate species alone. Evidence for a more general principle in other brain areas and other mammalian species can be found in the literature as well (Borowsky and Collins, 1989; Patel, 1983; Tuor et al., 1994; Woolsey et al., 1996).

Qualitative Aspects

The general organization of the cortical vasculature of macaque monkeys as assessed by the corrosion cast technique is comparable to that described for other primates like e.g. the human (Duvernoy et al., 1981; Reina-De La Torre et al., 1998). Of interest for understanding the basic principles of blood flow regulation and the resulting fluid dynamic distribution of the blood stream are the characterization and localization of the elements that control the blood flow. We detected numerous perivascular, ring-like structures, the so-called plastic strips, in our corrosion cast preparations, all of which were found around arteries and near the surface or branching points. Their origin is still under debate (Aharinejad et al., 1990; Castenholz et al., 1982; Rodriguez-Baeza et al., 1998), but we support the idea that they stem from resin that infiltrates space that under physiological conditions is occupied by arterial smooth muscle cells arranged ring-like around the vessels. These might function as sphincters to regulate the local blood inflow, as proposed by others (Harrison et al., 2002;

Rodriguez-Baeza et al., 1998), although we were not able to detect a relevant amount of circular constrictions from such structures in our preparations, be it in corrosion casts or in immunostainings. This might be due to the perfusion pressure and the following fixation procedure, which possibly fix the sphincters in an open state. In vivo they probably are constricted by default to allow an increase in blood flow on demand. The perfusion conditions might also be responsible for the occurrence of such plastic strips around the vessels in corrosion cast preparations at all, because somehow these spaces had to be or had to become connected to the lumen of the vessel they surround; otherwise they would not have been filled with resin. Whether this connection exists in vivo and if so, which function it has, or if junctions in the blood brain barrier have been ruptured during the perfusion to allow the resin to enter these extraluminal spaces is a question that has to be answered yet.

There are more contractile elements that might be involved in the regulation of the cerebral blood flow than the sphincter-like perivascular structures described above, namely pericytes on capillaries (Peppiatt et al., 2006) and the smooth muscle sheaths of arteries which regulate the vascular resistance. The density and the localization of the entirety of blood-flow-regulating elements has to be assessed to contribute to the better estimation of a realistic vascular point spread function (Dunn et al., 2005; Logothetis and Wandell, 2004; Sheth et al., 2004; Sheth et al., 2005; Weber et al., 2004) , which would be an important improvement for the prediction of hemodynamic imaging signals.

Another valuable aspect of the corrosion cast preparations is the possibility to discriminate arteries from veins. The surplus of arteries found amongst the penetrating vessels in the macaque cortex is in accordance with recent data from marmoset monkeys (Guibert et al., 2010). This leads to the conclusion that in primates the

feeding territory of an artery is smaller than the draining volume of a vein. This limits the achievable spatial resolution of certain imaging sequences in BOLD fMRI to the spatial distribution of the respective main source of the signal. The frequently used gradient-echo echo-planar imaging (EPI) sequence is most sensitive to effects originating mainly near draining veins, which would according to the present data enable an ultimate spatial resolution of around 0.70 mm^3, the draining volume of a cortical vein, whereas imaging signals originating from arteries with a feeding volume of 0.44 mm^3 would provide a better spatial resolution. Of course, this rough estimate only holds true if CBF is regulated on the level of the first order cortical vessels running perpendicular to the cortical surface. The spatial resolution of spin-echo EPI sequences might be even superior to that since they are more sensitive to signals originating from the capillary bed (Goense et al., 2007; Goense and Logothetis, 2006; Harel et al., 2006; Lee et al., 1999; Yacoub et al., 2003).

Quantitative Aspects

Quantitative differences in vascular density between areas might have direct implications for imaging studies applying spin-echo EPI, especially given the fact that capillaries make up a high proportion of the total vascular volume. The blood volume fraction is used as a parameter in many models of the BOLD signal (Buxton et al., 1998; Buxton et al., 2004) without considering that differences might exist within or between cortical areas. We could show that such vascularization differences do exist between the primary and non-primary visual cortical areas in macaques (Weber et al., 2008). Less pronounced this effect was also seen in auditory and somatosensory cortex (unpublished data). Only recently it was reported that very short stimuli elicit a BOLD signal attributable mainly to the middle layers of the cortex, where the capillary density is highest (Hirano et al., 2011). The signal-to-noise ratio of the

hemodynamic signals might be increased in regions with a higher microvascular density due to which differences between conditions would be detected more easily there then in other regions with a lower microvascular density. The details of this relationship are still subject of further research, but nonetheless direct comparisons of signals measured in primary and non-primary sensory areas should be treated with caution.

Metabolic Aspects

What both our publications could confirm was the tight relationship between vascular density and steady-state oxidative metabolic demand represented by cytochrome oxidase (COX) activity. In all investigated subareas, namely the cortical layers as well as blobs and interblobs, the local correlation between COX activity and capillary density was strong. This supports the findings of earlier studies, though most of them did not examine this aspect in a strictly quantitative way (Cox et al., 1993; Fonta and Imbert, 2002; Riddle et al., 1993; Tieman et al., 2004; Tuor et al., 1994; Woolsey et al., 1996; Zheng et al., 1991). A novelty of our studies is the finding that COX activity and vascular density seem to correlate in the same proportion, irrespective of the subregion or the orientation of the section. Although our investigations are restricted to the primary visual cortex, these results indicate a more general phenomenon. Several studies describe a local co-development of COX activity and vascularization during the postnatal development of the brain (Fonta and Imbert, 2002; Tieman et al., 2004) and it should be noted that the degree of metabolic activity establishes first, whereupon the vascularization adapts (Tuor et al., 1994). There is no straightforward answer to the question which of the cortical elements drives the metabolic need primarily. It is merely the net sum of the energy used by neurons, synapses and glia together that the total energy demand consists of. Theoretically the

individual composition of cortical elements at a certain location might differ significantly from another while both exhibit the same metabolic need and vascular density. However, the other way round different metabolic activity indicates different total amounts of energy consuming elements and therefore different anatomical properties.

Functional Aspects

The net sum of energy used by all cortical elements together constitutes the total metabolic need. Therefore, the element density is an important factor for the determination of the metabolic demand. But besides the quantity, the mean activity of the individual cortical elements does play a crucial role. The coincidence of increased COX activity with termination sites of thalamocortical afferents has been proposed and described already earlier and in several species and cortical areas (Borowsky and Collins, 1989; Ding and Casagrande, 1997; Ichinohe et al., 2003; Land and Erickson, 2005; Levitt et al., 1995; Livingstone and Hubel, 1982; Martin, 1988; Sincich and Horton, 2002; Wong-Riley, 1979). According to several authors the proportion of thalamocortical synapses from the total amount of synapses at a given site of direct thalamic projections only ranges from 5 to 15% (Ahmed et al., 1994; Benshalom and White, 1986; Garey and Powell, 1971; Latawiec et al., 2000). Most synapses are from corticocortical connections. If the number of these synapses is more or less constant, depending on the local neuronal density, and the synapses from the thalamic afferents come on top of this, one could assume that this additional synaptic activity causes the increase in metabolic activity. However, at least in the blobs the total number of synapses, including the thalamocortical ones from the LGN, does not differ from the surrounding interblob region (Carroll and Wong-Riley, 1984). The authors only find the proportion of highly reactive mitochondria compared to lighter stained ones

increased within the blobs, especially in asymmetrical synapses, but also in symmetrical ones as well as in neuronal somata. This speaks for a locally increased processing activity due to more excitatory influence, which might have its origin in the thalamic afferents. Despite their small number the impact of these afferents to the cortical network is significant (Douglas and Martin, 2007). This might be due to specific properties of the thalamic synapse, which has been proposed to be very powerful (Gil et al., 1999) or to the postsynaptic processing, like an eventual excitatory amplification by the target neurons (Stratford et al., 1996). Even if the efficacy of the individual thalamocortical synapse is low, synchronicity of numerous convergent inputs from thalamic projections could drive cortical activation, without any further intracortical amplification (Bruno and Sakmann, 2006). The exact type of pre- or postsynaptic processes and properties responsible for the strong influences of the thalamic projections on the cortex are unclear. However, it is undisputed that these features cause an increased level of oxidative metabolism as compared to sites without direct thalamic input.

Concluding Remarks

The quantification of the vascularization in the primate visual cortex provides important benchmark data for the modeling and prediction of hemodynamic imaging signals. But another and more general finding might be of more general relevance. The tightly interrelated trinity of vascular density, cytochrome oxidase activity and direct thalamic projection might give rise to useful methodological approaches for further research concerning one of these or related fields. If the fixed proportional relationship between vascular density and COX activity can be consolidated further, the exact quantification of the vasculature in the primate visual cortex could be used to calibrate measurements of COX staining intensity in other primate brain areas. This

could be used as a reference for researchers performing hemodynamic imaging studies to get advice where different signal strengths might be biased by differences in vascular density. Eventually this concerns all studies, which include measurements from primary sensory areas, as these receive afferents from the thalamus, which in turn might coincide with increased COX activity and therefore vascular density.

Outlook

Many loose ends remain and the presented work might give inspiration to further research. First of all, the qualitative and quantitative assessment of the vasculature should be extended to other brain areas and other species to clarify the question of how general the described results can be ranked. Especially knowledge about potential differences in vascular organization between the main model organisms in animal research - the rodents and the primates - would be of great importance. Another interesting aspect in the context of interspecies comparisons would be the confirmation of the possibly proportional relationship of COX activity and vascular density in general. An extensive evaluation of relative COX activity might substitute the exact measurement of vascular density in large-scale areas of the brain. But before that this relation needs to be confirmed in other species and brain areas. The third facet concerns the thalamic afferents. By the usage of antibodies against thalamocortical axon terminals like the vesicular glutamate transporter VGluT2 (Fremeau, Jr. et al., 2001; Kaneko and Fujiyama, 2002), cytochrome oxidase-rich areas could be systematically investigated for the presence of direct thalamic input to clarify this relationship once and for all.

However, the most promising prospect arises from another technique, which has the ability to combine the advantages of the methods used so far, without suffering from their drawbacks. This is the synchrotron-radiation based x-ray microscopy (srXTM) which allows the tomographic assessment of the vascular topology in a large field of view with a spatial resolution that is sufficient to reliably detect all blood vessels down to capillary size (Heinzer et al., 2006; Plouraboue et al., 2004). The 3-

dimensional data obtained through this approach enables deeper insights into the mechanisms of cortical angiogenesis (Risser et al., 2009) and provides important parameters for the fluid dynamic modeling of cerebral blood flow control (Reichold et al., 2009). A first set of experiments from our lab in collaboration with the Synchrotron Light Source (SLS) at the Paul-Scherrer-Institut in Villigen, Switzerland, was published already (Reichold et al., 2009). In a second run, more and qualitatively better data was acquired, due to many improvements in sample preparation, data acquisition and data analysis. The current procedure for sample preparation for example permits the differentiation of arteries and veins and therefore the discrete examination of the topology of arterial and venous vessel trees, like their branching patterns or their spatial coverage. The image acquisition time could be reduced and the switching of the samples became automated which taken together enabled an enormous increase in the number of samples that were scanned and the amount of data that was acquired. Revised algorithms for processing of the data were needed to deal with the huge new dataset. Our first preliminary results from this 3-dimensional approach to the investigation of the cortical vasculature confirm the results from the other techniques used and described herein (Keller et al., 2011; Weber et al., 2008), which leaves us confident about their reliability and the reliability of the results yet to come.

Reference List

Aharinejad,S., Lametschwandtner,A., Holtl,W., and Firbas,W. (1990). The microvasculature of the guinea pig ureter. A scanning electron microscopic investigation. Scanning Microsc. *4*, 957-965.

Ahmed,B., Anderson,J.C., Douglas,R.J., Martin,K.A., and Nelson,J.C. (1994). Polyneuronal innervation of spiny stellate neurons in cat visual cortex. J Comp Neurol. *341*, 39-49.

Benshalom,G., and White,E.L. (1986). Quantification of thalamocortical synapses with spiny stellate neurons in layer IV of mouse somatosensory cortex. J Comp Neurol. *253*, 303-314.

Blinder,P., Shih,A.Y., Rafie,C., and Kleinfeld,D. (2010). Topological basis for the robust distribution of blood to rodent neocortex. Proc. Natl. Acad. Sci. U. S. A *107*, 12670-12675.

Borowsky,I.W., and Collins,R.C. (1989). Metabolic Anatomy of Brain - A Comparison of Regional Capillary Density, Glucose-Metabolism, and Enzyme-Activities. Journal of Comparative Neurology *288*, 401-413.

Braitenberg,V., and Schüz,A. (1991). Cortex: Statistics and Geometry of Neuronal Connectivity (Heidelberg: Springer).

Bruno,R.M., and Sakmann,B. (2006). Cortex is driven by weak but synchronously active thalamocortical synapses. Science *312*, 1622-1627.

Bugge,J. (1985). The Evolution of the Cephalic Arterial System in Mammals. Fortschritte der Zoologie *30*, 405-408.

Butler,H. (1967). Development of Mammalian Dural Venous Sinuses with Especial Reference to Post-Glenoid Vein. Journal of Anatomy *102*, 33-&.

Buxton,R.B., Uludag,K., Dubowitz,D.J., and Liu,T.T. (2004). Modeling the hemodynamic response to brain activation. Neuroimage *23 Suppl 1*, S220-S233.

Buxton,R.B., Wong,E.C., and Frank,L.R. (1998). Dynamics of blood flow and oxygenation changes during brain activation: the balloon model. Magn Reson. Med. *39*, 855-864.

Carroll,E.W., and Wong-Riley,M.T. (1984). Quantitative light and electron microscopic analysis of cytochrome oxidase-rich zones in the striate cortex of the squirrel monkey. J. Comp Neurol. *222*, 1-17.

Castenholz,A., Zoltzer,H., and Erhardt,H. (1982). Structures imitating myocytes and pericytes in corrosion casts of terminal blood vessels. A methodical approach to the phenomenon of "plastic strips" in SEM. Mikroskopie. *39*, 95-106.

Cox,S.B., Woolsey,T.A., and Rovainen,C.M. (1993). Localized dynamic changes in cortical blood flow with whisker stimulation corresponds to matched vascular and neuronal architecture of rat barrels. J Cereb Blood Flow Metab *13*, 899-913.

Ding,Y., and Casagrande,V.A. (1997). The distribution and morphology of LGN K pathway axons within the layers and CO blobs of owl monkey V1. Visual Neuroscience *14*, 691-704.

Douglas,R.J., and Martin,K.A. (2007). Mapping the matrix: the ways of neocortex. Neuron *56*, 226-238.

Drake,C.T., and Iadecola,C. (2007). The role of neuronal signaling in controlling cerebral blood flow. Brain and Language *102*, 141-152.

Dunn,A.K., Devor,A., Dale,A.M., and Boas,D.A. (2005). Spatial extent of oxygen metabolism and hemodynamic changes during functional activation of the rat somatosensory cortex. Neuroimage *27*, 279-290.

Duvernoy,H.M., Delon,S., and Vannson,J.L. (1981). Cortical blood vessels of the human brain. Brain Res. Bull. *7*, 519-579.

Fitzpatrick,D., Itoh,K., and Diamond,I.T. (1983). The Laminar Organization of the Lateral Geniculate-Body and the Striate Cortex in the Squirrel-Monkey (Saimiri-Sciureus). Journal of Neuroscience *3*, 673-702.

Fonta,C., and Imbert,M. (2002). Vascularization in the primate visual cortex during development. Cereb Cortex *12*, 199-211.

Fremeau,R.T., Jr., Troyer,M.D., Pahner,I., Nygaard,G.O., Tran,C.H., Reimer,R.J., Bellocchio,E.E., Fortin,D., Storm-Mathisen,J., and Edwards,R.H. (2001). The expression of vesicular glutamate transporters defines two classes of excitatory synapse. Neuron *31*, 247-260.

Fukuda,S., Fini,C.A., Mabuchi,T., Koziol,J.A., Eggleston,L.L., Jr., and del Zoppo,G.J. (2004). Focal cerebral ischemia induces active proteases that degrade microvascular matrix. Stroke *35*, 998-1004.

Garey,L.J., and Powell,T.P. (1971). An experimental study of the termination of the lateral geniculo-cortical pathway in the cat and monkey. Proc. R. Soc. Lond B Biol. Sci. *179*, 41-63.

Gil,Z., Connors,B.W., and Amitai,Y. (1999). Efficacy of thalamocortical and intracortical synaptic connections: Quanta, innervation, and reliability. Neuron *23*, 385-397.

Goense,J.B., and Logothetis,N.K. (2006). Laminar specificity in monkey V1 using high-resolution SE-fMRI. Magn Reson. Imaging *24*, 381-392.

Goense,J.B., Zappe,A.C., and Logothetis,N.K. (2007). High-resolution fMRI of macaque V1. Magn Reson. Imaging *25*, 740-747.

Guibert,R., Fonta,C., and Plouraboue,F. (2010). Cerebral blood flow modeling in primate cortex. J. Cereb. Blood Flow Metab *30*, 1860-1873.

Harel,N., Lin,J., Moeller,S., Ugurbil,K., and Yacoub,E. (2006). Combined imaging-histological study of cortical laminar specificity of fMRI signals. Neuroimage *29*, 879-887.

Harrison,R.V., Harel,N., Panesar,J., and Mount,R.J. (2002). Blood capillary distribution correlates with hemodynamic-based functional imaging in cerebral cortex. Cereb Cortex *12*, 225-233.

Haug,H. (1986). History of neuromorphometry. J Neurosci. Methods *18*, 1-17.

Heinzer,S., Krucker,T., Stampanoni,M., Abela,R., Meyer,E.P., Schuler,A., Schneider,P., and Muller,R. (2006). Hierarchical microimaging for multiscale analysis of large vascular networks. Neuroimage *32*, 626-636.

Hevner,R.F., Liu,S., and Wong-Riley,M.T. (1995). A metabolic map of cytochrome oxidase in the rat brain: histochemical, densitometric and biochemical studies. Neuroscience *65*, 313-342.

Hirano,Y., Stefanovic,B., and Silva,A.C. (2011). Spatiotemporal evolution of the functional magnetic resonance imaging response to ultrashort stimuli. J. Neurosci. *31*, 1440-1447.

Horton,J.C., and Hubel,D.H. (1981). Regular Patchy Distribution of Cytochrome-Oxidase Staining in Primary Visual-Cortex of Macaque Monkey. Nature *292*, 762-764.

Iadecola,C., and Nedergaard,M. (2007). Glial regulation of the cerebral microvasculature. Nature Neuroscience *10*, 1369-1376.

Ichinohe,N., Fujiyama,F., Kaneko,T., and Rockland,K.S. (2003). Honeycomb-like mosaic at the border of layers 1 and 2 in the cerebral cortex. Journal of Neuroscience *23*, 1372-1382.

Jolivet,R., Magistretti,P.J., and Weber,B. (2009). Deciphering neuron-glia compartmentalization in cortical energy metabolism. Front Neuroenergetics. *1*, 4.

Kaneko,T., and Fujiyama,F. (2002). Complementary distribution of vesicular glutamate transporters in the central nervous system. Neurosci. Res. *42*, 243-250.

Keller,A.L., Schuz,A., Logothetis,N.K., and Weber,B. (2011). Vascularization of cytochrome oxidase-rich blobs in the primary visual cortex of squirrel and macaque monkeys. J Neurosci. *31*, 1246-1253.

Land,P.W., and Erickson,S.L. (2005). Subbarrel domains in rat somatosensory (S1) cortex. J Comp Neurol. *490*, 414-426.

Latawiec,D., Martin,K.A., and Meskenaite,V. (2000). Termination of the geniculocortical projection in the striate cortex of macaque monkey: a quantitative immunoelectron microscopic study. J Comp Neurol. *419*, 306-319.

Lee,S.P., Silva,A.C., Ugurbil,K., and Kim,S.G. (1999). Diffusion-weighted spin-echo fMRI at 9.4 T: microvascular/tissue contribution to BOLD signal changes. Magn Reson. Med. *42*, 919-928.

Levitt,J.B., Yoshioka,T., and Lund,J.S. (1995). Connections between the pulvinar complex and cytochrome oxidase-defined compartments in visual area V2 of macaque monkey. Exp. Brain Res. *104*, 419-430.

Livingstone,M.S., and Hubel,D.H. (1982). Thalamic inputs to cytochrome oxidase-rich regions in monkey visual cortex. Proc. Natl. Acad. Sci. U. S. A *79*, 6098-6101.

Logothetis,N.K., and Wandell,B.A. (2004). Interpreting the BOLD signal. Annu. Rev. Physiol *66*, 735-769.

Martin,K.A. (1988). From enzymes to visual perception: a bridge too far? Trends Neurosci. *11*, 380-387.

Miodonski,A., Hodde,K.C., and Bakker,C. (1976). Rasterelektronenmikroskopie von Plastil-Korrosions-Präparaten: morphologische Unterschiede zwischen Arterien und Venen. Beitr. Elektronenmikroskop. Direktabb. Oberfl. *9*, 435-442.

Nehlig,A. (1996). Metabolism of the central nervous system. In Neurophysiological Basis of Cerebral Blood Flow Control: An Introduction, S. Mraovitch, and R. Sercombe, eds. (London: John Libbey & Company), pp. 177-196.

O'Kusky,J., and Colonnier,M. (1982). A laminar analysis of the number of neurons, glia, and synapses in the adult cortex (area 17) of adult macaque monkeys. J. Comp Neurol. *210*, 278-290.

Ogawa,S., Lee,T.M., Kay,A.R., and Tank,D.W. (1990). Brain magnetic resonance imaging with contrast dependent on blood oxygenation. Proc. Natl. Acad. Sci. U. S. A *87*, 9868-9872.

Patel,U. (1983). Non-random distribution of blood vessels in the posterior region of the rat somatosensory cortex. Brain Res. *289*, 65-70.

Peppiatt,C.M., Howarth,C., Mobbs,P., and Attwell,D. (2006). Bidirectional control of CNS capillary diameter by pericytes. Nature *443*, 700-704.

Plouraboue,F., Cloetens,P., Fonta,C., Steyer,A., Lauwers,F., and Marc-Vergnes,J.P. (2004). X-ray high-resolution vascular network imaging. J Microsc. *215*, 139-148.

Reichold,J., Stampanoni,M., Lena Keller,A., Buck,A., Jenny,P., and Weber,B. (2009). Vascular graph model to simulate the cerebral blood flow in realistic vascular networks. J Cereb Blood Flow Metab *29*, 1429-1443.

Reina-De La Torre,F., Rodriguez-Baeza,A., and Sahuquillo-Barris,J. (1998). Morphological characteristics and distribution pattern of the arterial vessels in human cerebral cortex: a scanning electron microscope study. Anat. Rec. *251*, 87-96.

Riddle,D.R., Gutierrez,G., Zheng,D., White,L.E., Richards,A., and Purves,D. (1993). Differential metabolic and electrical activity in the somatic sensory cortex of juvenile and adult rats. J Neurosci. *13*, 4193-4213.

Ridge,J.W. (1967). Distribution of Cytochrome-Oxidase Activity in Rabbit Brain. Biochemical Journal *102*, 612-&.

Risser,L., Plouraboue,F., Cloetens,P., and Fonta,C. (2009). A 3D-investigation shows that angiogenesis in primate cerebral cortex mainly occurs at capillary level. Int. J Dev. Neurosci. *27*, 185-196.

Rodriguez-Baeza,A., Reina-De La,T.F., Ortega-Sanchez,M., and Sahuquillo-Barris,J. (1998). Perivascular structures in corrosion casts of the human central nervous system: a confocal laser and scanning electron microscope study. Anat. Rec. *252*, 176-184.

Sheth,S.A., Nemoto,M., Guiou,M., Walker,M., Pouratian,N., and Toga,A.W. (2004). Linear and nonlinear relationships between neuronal activity, oxygen metabolism, and hemodynamic responses. Neuron *42*, 347-355.

Sheth,S.A., Nemoto,M., Guiou,M.W., Walker,M.A., and Toga,A.W. (2005). Spatiotemporal evolution of functional hemodynamic changes and their relationship to neuronal activity. J Cereb Blood Flow Metab *25*, 830-841.

Sincich,L.C., and Horton,J.C. (2002). Pale cytochrome oxidase stripes in V2 receive the richest projection from macaque striate cortex. J. Comp Neurol. *447*, 18-33.

Stratford,K.J., Tarczy-Hornoch,K., Martin,K.A., Bannister,N.J., and Jack,J.J. (1996). Excitatory synaptic inputs to spiny stellate cells in cat visual cortex. Nature *382*, 258-261.

Tieman,S.B., Mollers,S., Tieman,D.G., and White,J. (2004). The blood supply of the cat's visual cortex and its postnatal development. Brain Res. *998*, 100-112.

Tsai,P.S., Kaufhold,J.P., Blinder,P., Friedman,B., Drew,P.J., Karten,H.J., Lyden,P.D., and Kleinfeld,D. (2009). Correlations of neuronal and microvascular densities in murine cortex revealed by direct counting and colocalization of nuclei and vessels. J Neurosci. *29*, 14553-14570.

Tuor,U.I., Kurpita,G., and Simone,C. (1994). Correlation of local changes in cerebral blood flow, capillary density, and cytochrome oxidase during development. J Comp Neurol. *342*, 439-448.

Weber,B., Burger,C., Wyss,M.T., von Schulthess,G.K., Scheffold,F., and Buck,A. (2004). Optical imaging of the spatiotemporal dynamics of cerebral blood flow and oxidative metabolism in the rat barrel cortex. Eur. J Neurosci. *20*, 2664-2670.

Weber,B., Keller,A.L., Reichold,J., and Logothetis,N.K. (2008). The microvascular system of the striate and extrastriate visual cortex of the macaque. Cereb. Cortex *18*, 2318-2330.

Wong-Riley,M. (1979). Changes in the visual system of monocularly sutured or enucleated cats demonstrable with cytochrome oxidase histochemistry. Brain Res. *171*, 11-28.

Woolsey,T.A., Rovainen,C.M., Cox,S.B., Henegar,M.H., Liang,G.E., Liu,D., Moskalenko,Y.E., Sui,J., and Wei,L. (1996). Neuronal units linked to microvascular modules in cerebral cortex: response elements for imaging the brain. Cereb Cortex *6*, 647-660.

Yacoub,E., Duong,T.Q., Van De Moortele,P.F., Lindquist,M., Adriany,G., Kim,S.G., Ugurbil,K., and Hu,X. (2003). Spin-echo fMRI in humans using high spatial resolutions and high magnetic fields. Magn Reson. Med. *49*, 655-664.

Zheng,D., Lamantia,A.S., and Purves,D. (1991). Specialized Vascularization of the Primate Visual-Cortex. Journal of Neuroscience *11*, 2622-2629.

Acknowledgments

First of all I want to thank my supervisor Prof. Dr. Bruno Weber for the motivational working environment we always had and the great technical and scientific opportunities he made possible. I also have to thank Dr. Heinz Schwarz, Prof. Dr. Marco Stampanoni and especially Johannes Reichold for their invaluable support at different stages of my work.

Prof. Dr. Almut Schüz and Prof. Dr. Valentino Braitenberg deserve to be honored in particular for sharing the joy of curiosity and also for providing an isle of peace within the hectic pace of the institute. Matthias Valverde has to be named here as well, I thank him for being a friend for all these years.

I want to thank Prof. Dr. Nikos Logothetis for giving me the chance to work on my thesis in such a fruitful scientific environment.

I am very grateful to my parents and grandparents for their invaluable mental and not unnoticeable financial support, especially my mother for enabling so much. In discussions, my sister sometimes offered me insights from a completely different point of view, which interestingly were not contrary, but rather complementary and enhanced my way to work. I have to thank her for that.

At last I want to thank my dear Marcus Eberle for his great encouragement, for sharing his organizational skills with me and especially for his love.

Zusammenfassung

Die quantitative und qualitative Beurteilung der versorgenden Blutgefäße und der lokalen Kapillardichten im visuellen Cortex von Makaken und Totenkopfäffchen, sowie der Zusammenhang von Blutgefäßdichte und oxydativer Stoffwechselkapazität waren Gegenstand der Untersuchungen, die in dieser kumulativen Dissertationsschrift dargelegt werden. In zwei Publikationen wurden der Nachweis lokal unterschiedlicher Kapillardichten und deren Korrelation zur sauerstoffbasierten Stoffwechselaktivität erbracht.

Die Organisation der Blutversorgung im Gehirn wurde mit verschiedenen Techniken untersucht. Anhand von Ausgusspräparaten, die einen Negativabdruck des Blutgefäßsystems darstellen, konnten die Morphologie, die Anzahl und die Verteilung der zuführenden Arterien und der ableitenden Venen beschrieben werden, sowie ein Eindruck des generellen organisatorischen Aufbaus des Gefäßsystems gewonnen werden. In Hirnschnittpräparaten wurden die Blutgefäße immunhistochemisch markiert und mit einem fluoreszierenden Farbstoff visualisiert, eine ebenfalls fluoreszierende Kernfärbung derselben Präparate ermöglichte die zweifelsfreie hirnanatomische Verortung der untersuchten Gebiete. Eine weitere Färbetechnik zeigte die lokale Aktivität der Cytochrom c Oxidase, eines mitochondrialen Enzyms des oxydativen Stoffwechsels. Diese in Kombination mit der immunhistochemischen Blutgefäßfärbung durchgeführt ermöglichte die Korrelation von Stoffwechselaktivität und Gefäßdichte.

Grundsätzlich ähnelt die Gefäßarchitektur im Cortex des Affen der beim Menschen beschriebenen. Die Morphologie der großen Arterien und Venen, das

Verzweigungsmuster bis zur Kapillarebene, sowie Hinweise auf den Blutfluss regulierende Strukturen entsprechen denen anderer Primaten. Die Messung lokaler Gefäßdichten zeigte eine inhomogene Verteilung der Kapillaren, mit einer höheren Dichte in den mittleren kortikalen Schichten und einer insgesamt erhöhten Gefäßdichte im primären visuellen Areal V1. Es zeigte sich auch, dass speziell die Kapillardichte gut mit der Aktivität der Cytochromoxidase korreliert, nicht nur über die kortikalen Schichten hinweg, sondern auch in anderen, durch eine erhöhte Cytochromoxidase-Aktivität auffällige Bereiche im primären visuellen Cortex, den sogenannten "Blobs". Dies könnte auf einen möglicherweise proportionalen Zusammenhang zwischen oxydativer Stoffwechselaktivität und Blutgefäßdichte hindeuten.

Insgesamt bleibt festzuhalten, dass Unterschiede in der Dichte der Blutgefäße im Cortex existieren, speziell die primären sensorischen Bereiche scheinen hier stärker versorgt zu sein. Dies könnte Einfluss auf die modernen, funktionellen hämodynamischen Bildgebungsverfahren haben, deren Signale aus der Blutbahn stammen und somit den Randbedingungen der Anatomie des Systems unterworfen sind. Bei der Interpretation solcher Messungen wird häufig vereinfacht von einer homogenen Durchblutung ausgegangen, doch vor allem bei Vergleichen zwischen primären und nicht-primären sensorischen Arealen könnte diese Annahme zu falschen Schlüssen führen. Die vorliegenden Ergebnisse könnten einer realistischeren Einschätzung der messbaren hämodynamischen Phänomene zuträglich sein.

Publication #1

Cerebral Cortex October 2008;18:2318–2330
doi:10.1093/cercor/bhm259
Advance Access publication January 24, 2008

The Microvascular System of the Striate and Extrastriate Visual Cortex of the Macaque

Bruno Weber[1,2], Anna Lena Keller[1], Johannes Reichold[3] and Nikos K. Logothetis[1]

[1]Max-Planck Institut für biologische Kybernetik, Spemannstr. 38, 72076 Tübingen, Germany, [2]University of Zurich, Institute for Pharmacology and Toxicology, Rämistrasse 100, 8091 Zurich, Switzerland and [3]Swiss Federal Institute of Technology, Institute for Fluid Dynamics, Sonneggstrasse 3, 8092 Zurich, Switzerland

In functional neuroimaging, neurovascular coupling is used to generate maps of hemodynamic changes that are assumed to be surrogates of regional neural activation. The aim of this study was to characterize the microvascular system of the primate cortex as a basis for understanding the constraints imposed on a region's hemodynamic response by the vascular architecture, density, as well as area- and layer-specific variations. In the macaque visual cortex, an array of anatomical techniques has been applied, including corrosion casts, immunohistochemistry, and cytochrome oxidase (COX) staining. Detailed measurements of regional vascular length density, volume fraction, and surface density revealed a similar vascularization in different visual areas. Whereas the lower cortical layers showed a positive correlation between the vascular and cell density, this relationship was very weak in the upper layers. Synapse density values taken from the literature also displayed a very moderate correlation with the vascular density. However, the vascular density was strongly correlated with the steady-state metabolic demand as measured by COX activity. This observation suggests that although the number of neurons and synapses determines an upper bound on an area's integrative capacity, its vascularization reflects the neural activity of those subpopulations that represent a "default" mode of brain steady state.

Keywords: capillaries, cerebral blood flow, collagen, monkey, neuroimaging, primate

Introduction

Despite its relatively small size the brain consumes roughly a quarter of the body's total glucose and a fifth of the oxygen. The high energy demand in combination with the fact that brain tissues lack any substantial capacity to store energy requires a tight spatiotemporal control of the energy supply. Changes in neural activity are indeed followed by precisely controlled changes in hemodynamics, as hypothesized more than a century ago (Mosso 1881; Roy and Sherrington 1890). This remarkable site- and time-specific neurovascular coupling has been systematically exploited to generate detailed maps of hemodynamic changes that are assumed to be surrogates of the actual regional neural activation. A recent celebrated example is the so-called blood oxygenation level–dependent (BOLD) contrast (Ogawa et al. 1990; Kwong et al. 1992) of magnetic resonance imaging (MRI), which reflects a complicated interplay of changes in blood volume, blood flow, and oxygen consumption (Logothetis and Wandell 2004). Because BOLD functional MRI (fMRI) is now the mainstay of biomedical neuroimaging, a lot of research has been focused recently on the functional aspects of neurovascular coupling, including the underlying signaling mechanisms, and the biochemistry of the neurometabolic link. Yet understanding neurometabolic and neurovascular coupling also requires a comprehension of the significant constraints imposed by architecture, density, and area-specific variation in the vascular system.

In response to this, a great deal of research is currently being devoted to understanding and modeling the link between neural activation and BOLD or perfusion fMRI (Logothetis et al. 2001; Devor et al. 2003; Jones et al. 2004; Sheth, Nemoto, Guiou, Walker, Pouratian, Toga, 2004; Thomsen et al. 2004; Martindale et al. 2005) or to describing the spatiotemporal dynamics of the hemodynamic response (Sheth, Nemoto, Guiou, Walker, Pouratian, Hageman, et al. 2004; Vanzetta et al. 2004; Weber et al. 2004; Sheth et al. 2005).

Ultimately, the spatial resolution and specificity of the hemodynamic response maps rely not only on the cascade of neurovascular signaling, but also on the vascular architecture and spatial level of blood flow regulation. Little is known, however, about the principles of flow regulation at different vascular scales, about the spatial distribution of vascular densities, and about the dependence of vasculature on cortical areas or brain sites in general. In their seminal study, Duvernoy et al. (1981) demonstrated area-specific vascular densities in the human brain, but unfortunately failed to provide precise quantitative data.

More recently, it was shown that areas with higher steady-state metabolic demand show a higher degree of vascular density (Zheng et al. 1991; Cox et al. 1993; Riddle et al. 1993; Woolsey et al. 1996; Tieman et al. 2004). In a study employing the corrosion cast technique together with optical imaging, Harrison et al. (2002) postulated a close relationship between the hemodynamic response map and both vascular density and the localization of perivascular flow control elements. All of these studies quantified the vasculature within a primary sensory area, or at best compared it with a secondary region. Investigations of a more complete hierarchical system—such as large parts of the visual system—have yet to be carried out. Because fMRI has the great advantage of measuring brain activity with full coverage, countless studies have compared the activity in different cortical areas. However, the completely different vascular densities and architectures of these regions would impede direct comparisons of the local readouts based on the hemodynamic response.

In this work, we describe and quantify the microvasculature in the macaque visual cortex, applying 2 different and complementary techniques. Scanning electron microscopy was used to image vascular corrosion casts for a qualitative assessment of the microvascular organization, for an estimation of the ratio between arteries and veins, as well as for an investigation of perivascular structures. At the same time,

double histochemical stains were performed on a large data set from 3 monkeys to evaluate quantitative layer- and area-specific vascular densities. To compare the vascular density with the basal metabolic demand of a given region, cytochrome oxidase (COX) stains were prepared in 3 additional subjects.

Materials and Methods

Animals

The brains of 7 adult monkeys (*Macaca mulatta*) were used in this study. The animals were involved in chronic combined physiological and behavioral experiments. At the end of the experiments and as part of our standard protocol the animals were killed with an overdose of pentobarbital (120 mg/kg). The euthanasia methods correspond to the guidelines of the "American Veterinary Association Panel on Euthanasia" and to the recommendations of the "Guide for the Care and Use of Laboratory Animals of the National Institutes of Health of the United States." They were all approved by the local authorities (Regierungspräsidium) and are also in full compliance with the guidelines of the European community (EUVD 86/609/EEC) for the care and use of laboratory animals. The brain of one of the animals was used for vascular corrosion casts, 3 brains were used for histochemical processing and 3 were stained for COX activity.

Vascular Corrosion Casts

The animal was perfused under deep sodium pentobarbital (120 mg/kg) anesthesia with 0.9% warm heparinized 0.1 M phosphate buffered saline (PBS) through a catheter in the ascending aorta. Then, Batson's #17 resin (Polysciences Inc., Eppelheim, Germany) was injected. After full polymerization overnight, the brain was carefully removed from the skull. The monkey brains were frozen at –20 °C and cut in cubes of about 15 × 15 × 15 mm using a dedicated saw. Brain tissue cubes were macerated in 5% KOH. The maceration process, which included daily rinses in water, took about 1 week. The polymer filling was then frozen in distilled water and the regions of interest were trimmed using a cryostat, yielding precise cuts without any damage of the fragile cast (see Figs 1 and 2). The specimens were then lyophilized overnight and sputter coated with gold. Scanning electron microscopy at 10–20 kV (Hitachi S-800) was then used to acquire high-resolution images of the vascular corrosion casts. Large vessels penetrating the cortex from the surface were individually imaged. On these high magnification images, each vessel could be identified as either an artery or a vein on the basis of the form of the imprints of the endothelial cell nuclei (Miodonski et al. 1976). As described before, arteries show shallow and elliptical or lens-shaped imprints. In contrast, the endothelial cell nuclei imprints on the venous lumen are more circular and the vessels have a more sluggish appearance due to the lower blood pressure in the venous system. In total, we analyzed 249 vessels that could be identified with sufficient certainty, from which we could estimate the ratio between arteries and veins. The shrinkage of the employed resin is known to be small (Lametschwandtner et al. 1990) and was disregarded in this study.

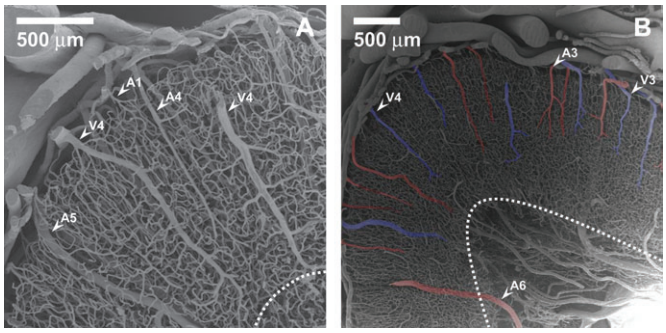

Figure 1. Scanning electron micrographs of a vascular corrosion cast from monkey visual cortex (superior temporal gyrus). Casts were cut and trimmed to allow a vertical view on the cortex. The gray–white matter demarcation line is shown as dashed line. Note the continuous orderly distribution of large vessels oriented perpendicularly to the cortical surface, their different length and branching patterns and the rather homogeneous mesh size and density of the capillary bed. The arrowheads in (*A*) and (*B*) exemplify a few vessel types, named according to the different vessel classes introduced by Duvernoy et al. (1981) for the human brain. According to this classification, a vessel of class 1 would for example feed/drain the capillary bed in the vascular layer 1, whereas a class 6 artery would traverse the cortex without any branching in gray matter. In Figure 1*B*, the larger penetrating arteries are shaded red and the veins are shaded blue. (A = artery, V = vein, 1–6 = category based on their cortical depth; scale bars = 500 µm.)

Histochemistry

Three animals were perfused transcardially under deep sodium pentobarbital (120 mg/kg) anesthesia with 8 L of warm heparinized 0.1 M PBS, followed by 2 L of cold 1% paraformaldehyde (PFA) in 0.1 M phosphate buffer (PB), then 4 L of 4% PFA in 0.1 M PB, and finally 1–2 L of 10% sucrose in 0.1 M PB. The brain was removed from the skull and stored in 4% PFA at 4 °C. Before sectioning, cortical blocks were placed in ascending concentrations of sucrose in 0.1 M PB (10%, 20%, and 30%) until they sank. Sixty-micrometer-thick horizontal frozen sections were then cut serially on a sliding microtome (Microm HM 440E, Walldorf, Germany) and stored at –20 °C in cryoprotectant (30% ethylene glycol and 10% sucrose in 0.05 M PB) until further processing. Double fluorescence histochemical staining was carried out on every tenth free-floating section. Sections were rinsed 3 times for 5 min each in 0.1 M PBS before and after antigen retrieval (incubation overnight in 0.05 M TRIS buffer at 65 °C). They were then blocked with TRIS saline pH 7.4 (0.6% TRIS) containing 0.02% sodium azide, 5% dry milk, 1% Triton X-100 (Sigma, Schnelldorf, Germany), and 1% goat serum for 1 h at room temperature. Anticollagen has been successfully used to stain all types of cerebral vessels (arteries, capillaries, and veins) with excellent specificity (Hamann et al. 1995; Fukuda et al. 2004). The primary antibody (monoclonal anticollagen type IV, clone col-94; Sigma) was diluted 1:500 in TRIS saline containing 2% bovine serum albumin (albumin bovine fraction V powder, Sigma), 0.05% thimerosal (Sigma), and 1% Triton X-100 and the sections were incubated in this solution overnight at 4° C. They were then washed again 3 times in 0.1 M PBS before being incubated overnight at 4 °C in the dark in a solution containing the secondary antibody (Cy-3–conjugated goat anti-mouse IgG (H + L), Jackson ImmunoResearch, West Grove, PA, diluted 1:500 in PBS containing 1% goat serum). In between 2 series of 3 rinses in 0.1 M PBS the sections were incubated for 5 min in 0.4 × 10^{-3}‰ DAPI (4′,6-diamidino-2-phenylindole dihydrochloride; Sigma) in dH_2O. Stained sections were mounted on glass slides and cover-slipped with polyvinyl alcohol (Mowiol 4-88; Hoechst, Frankfurt, Germany) containing 4% 1,4-diazobicyclooctane (Merck, Darmstadt, Germany) as an antifading reagent. Consecutive sections were stained for Nissl and myelin (Werner'sche Markscheidenfärbung). The tissue shrinkage due to the perfusion and fixation was assumed to be minimal. The shrinkage produced by subsequent tissue handling was measured according to the protocol described in O'Kusky and Colonnier (1982), and was found to be 5%. It is important to note that this value is rather small due to the fact that the sections were not dry-mounted.

Fluorescence Microscopy

Cy-3 and DAPI images of identical fields of view were acquired using a fluorescence microscope (Axiophot, 5× objective; Carl Zeiss, Göttingen, Germany) equipped with a CCD camera (Axiocam MRm, controlled by Axiovision 4.3; Zeiss, Göttingen, Germany).

Data Analysis

Measurements were made on images extending from cortical layer I to white matter (approximately 1 × 2 mm in size). The specific cortical visual areas were identified with the help of an anatomic atlas (Saleem and Logothetis 2006). Within a visual area, images were taken from locations without obvious histological damage. All digital image processing was performed using Matlab (Mathworks, Natick, MA). The raw anticollagen images (Fig. 3*C,E*) were median filtered and thresholded to yield binary images of the vessels (Fig. 3*D,F*). The total projected vessel length was computed on the eroded traces (Fig. 3*G*). The volume fraction (%), length density (mm/mm^3), surface density (mm^2/

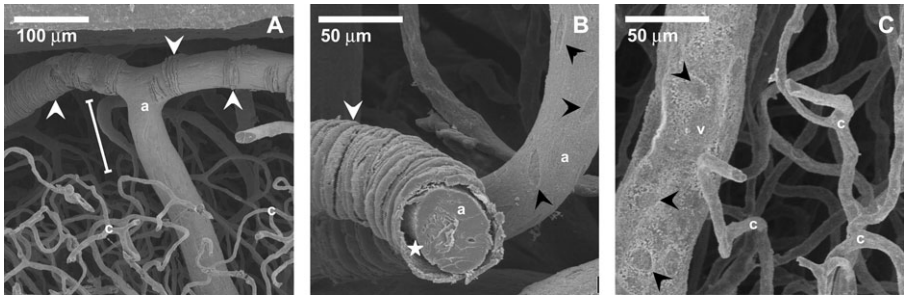

Figure 2. Details of coronal view on a vascular corrosion cast from monkey visual cortex. (*A*) Superficial artery with perivascular elements, so-called plastic strips. The white bar marks the upper molecular layer which is devoid of capillaries. (*B*) Plastic strip surrounding artery. Note the gap between the vessel lumen and the plastic strip (asterisk). Alongside this vessel runs another artery without plastic strips, showing the typical elongated imprints of arterial endothelial cell nuclei. (*C*) Vein with circular imprints of endothelial cell nuclei, in contrast to the longish arterial ones. (White arrowheads = plastic strips; black arrowheads = imprints of endothelial nuclei, a = artery, v = vein, c = capillary.)

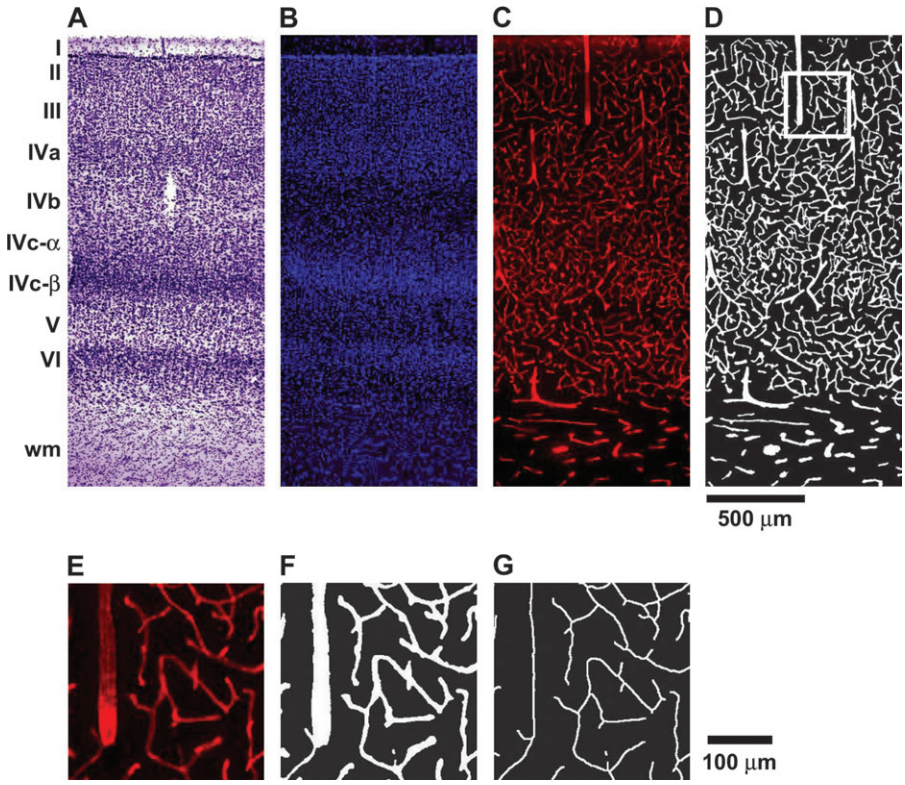

Figure 3. Double fluorescence stainings of the macaque visual area V1. (*A*) Nissl stain, with easily identifiable laminae of striate cortex (wm = white matter), consecutive section to (*B–G*); (*B*) DAPI stain used for identification of cortical laminae, note the good correspondence of cell nuclei density to Nissl stain; (*C*) raw image of a Cy-3 anticollagen type IV stain used for the quantification of the vessels (*B* and *C* identical sections); (*D*) Filtered and thresholded binary vessel image (same as *B*); (*E–G*) magnified subarea indicated in (*D*) to illustrate image quality; (*G*) eroded trace of binary vessel image.

mm^3), and mean vessel diameter (μm) were then computed stereologically (taking into account the bias induced by the finite section thickness; Russ and Dehoff 2000; see Appendix for details of the quantification assumptions and methods) for regions of interest (ROIs) representing the cortical layers. The density and diameter values were separately assessed for capillaries and the remaining vessels (noncapillaries) on the basis of a diameter threshold. Vessels with a diameter < 8 μm were considered to be capillaries. A threshold of 8 μm is an appropriate standard value well within the range of values used in other studies (Stewart et al. 1997; Michaloudi et al. 2005, and references therein).

For a semiquantitative estimation of cell density, the DAPI images were converted into 8-bit gray values and the gray values were taken as a relative measure of cell density (including all cell types). This analysis was restricted to V1.

Layer-specific ROIs (for the striate cortex: layers I, II, III, IVa, IVb, IVc-α, IVc-β, V, VI; for the extrastriate cortex: layers I, II/III, IV, V, VI) were drawn manually on the corresponding DAPI image (Fig. 3*B*) and were confirmed on the consecutive Nissl (Fig. 3*A*) and myelin stains. The mean depth of the center of mass of each layer-specific ROI is shown in Figures 4 and 5. Differences between area- and layer-specific measures were statistically analyzed using analyses of variance (ANOVAs) and Tukey post hoc tests using SPSS (SPSS, Inc., Chicago, IL). For comparisons between striate and extrastriate cortex, an ROI was drawn in V1 including all layer IV subdivisions and layers II and III were pooled.

COX Staining

Three animals were perfused as described above, with all consecutive steps kept as short as possible to preserve maximal obtainable oxidase activity. The visual cortices were dissected immediately after removal of the brain and cryoprotected in 10%, 20%, and 30% sucrose solution

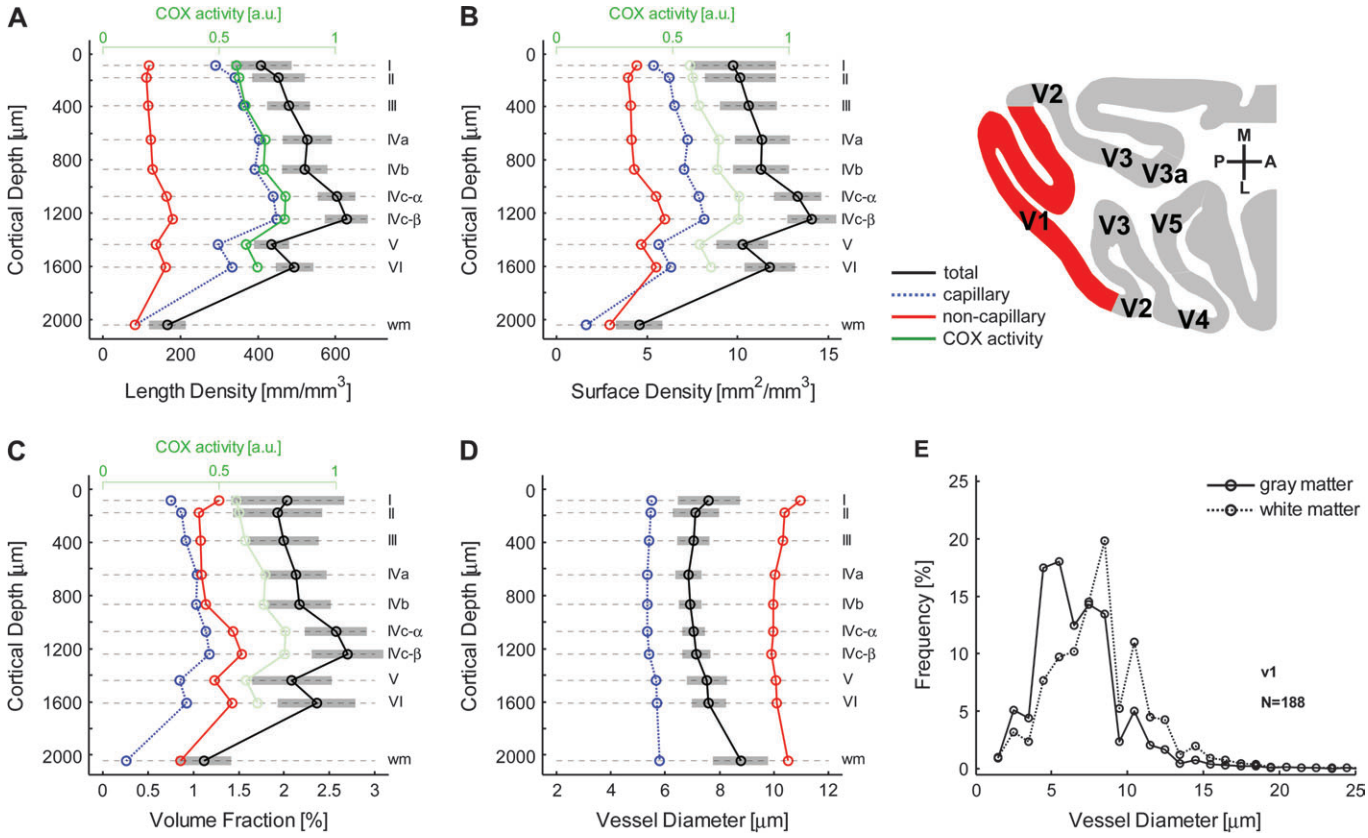

Figure 4. Lamina- and area-specific vascular density in visual area V1. Quantitative values of microvascular system across the cortical layers and cortical depths (µm from cortical surface) in the striate cortex. The black traces show the overall mean density (±standard deviation indicated with gray shaded area). The blue trace shows the values for the capillaries and the red for the noncapillary vessels. The green trace represents the COX activity in arbitrary units. Data for the microvascular parameters and the COX activity stem from different animals. (*B* and *C*) The COX data shown in (*A*) are replotted with transparent lines and symbols to facilitate comparison while affecting legibility as little as possible. (*A*) Length density in mm/mm^3. (B) Surface density in mm^2/mm^3. (*C*) Volume fraction in percent. (*D*) Average vessel diameters in µm. (*E*) Frequency distribution of vessel calibers for gray and white matter.

until they sank and then 60-µm-thick sections were cut horizontally. The sections were further processed for cytochrome *c* oxidase staining (Wong-Riley 1979, 1989; Wong-Riley and Welt 1980; Carroll and Wong-Riley 1984), and the rest of the brains were stored in 4% PFA. After washing in 0.1 M PB, the sections were incubated free floating and with light agitation at 37 °C in a solution consisting of 0.05% DAB (3,3′ diaminobenzidine tetrahydrochloride), 0.04% cytochrome *c* from horse heart, and 3% sucrose (all from Sigma) in 0.1 M PB under regular visual control until sufficient contrast was achieved. The reaction was stopped with 3 subsequent washing steps in 0.1 M PB and the sections were then mounted and cover-slipped as described above for the immunohistochemically stained sections.

Images were acquired using a microscope (Axiophot, 5× objective; Carl Zeiss, Göttingen, Germany) equipped with a CCD camera (Axiocam MRm, controlled by Axiovision 4.3; Zeiss, Göttingen, Germany). The images were converted into 8-bit gray values, the inverted gray values of the cortex were taken as a relative measure for oxidative metabolism (Wong-Riley 1979, 1989; Wong-Riley and Welt 1980; Carroll and Wong-Riley 1984). In V1, layer-specific ROIs were defined visually on the COX stains and were confirmed on the consecutive Nissl stain. The relationship between the layer-specific vascular densities and the cytochrome activities was statistically tested using the Spearman rank correlation.

Results

Corrosion Casts

The general organization of the cortical vasculature as described thoroughly by Duvernoy et al. (1981) in the human brain can also be identified in the vascular casts from the macaque monkey brain (see Figs 1 and 2). Large vessels are localized on the surface of the brain and the cortical arteries and veins are oriented perpendicular to the surface. Arteries are easily identified by their elongated imprints of the endothelial cell nuclei. These imprints appear more circular in the case of venous vessels. Large penetrating arteries were more numerous than veins; the ratio was found to be 1:~1.6 (number of identified vessels: 249). The total area of the analyzed tangential views was 33.7 mm^2. By dividing this area by the number of penetrating large vessels (132 arteries and 82 veins), we were able to determine the mean area irrigated or drained by the vessels to be 0.26 and 0.41 mm^2 for arteries and veins, respectively. Assuming a cylindrical volume and a mean cortical thickness of 1.7 mm, we can estimate an average irrigation volume of 0.44 mm^3 for large penetrating arteries and an average draining volume of 0.70 mm^3 for large cortical veins.

The cortical arteries themselves branch and give rise to a fine capillary network also called the capillary bed. The vascular density is markedly higher in gray than in white matter. However, within the cortex a continuous orderly pattern can be observed with only moderate changes in vascular density. Figure 2 shows the so-called plastic strips around arteries that have been reported by several authors (Castenholz et al. 1982; Aharinejad et al. 1990; Rodriguez-Baeza et al. 1998). As described before, these structures are not tightly connected to the vessel lumen (Fig. 2*B*). Most of these perivascular

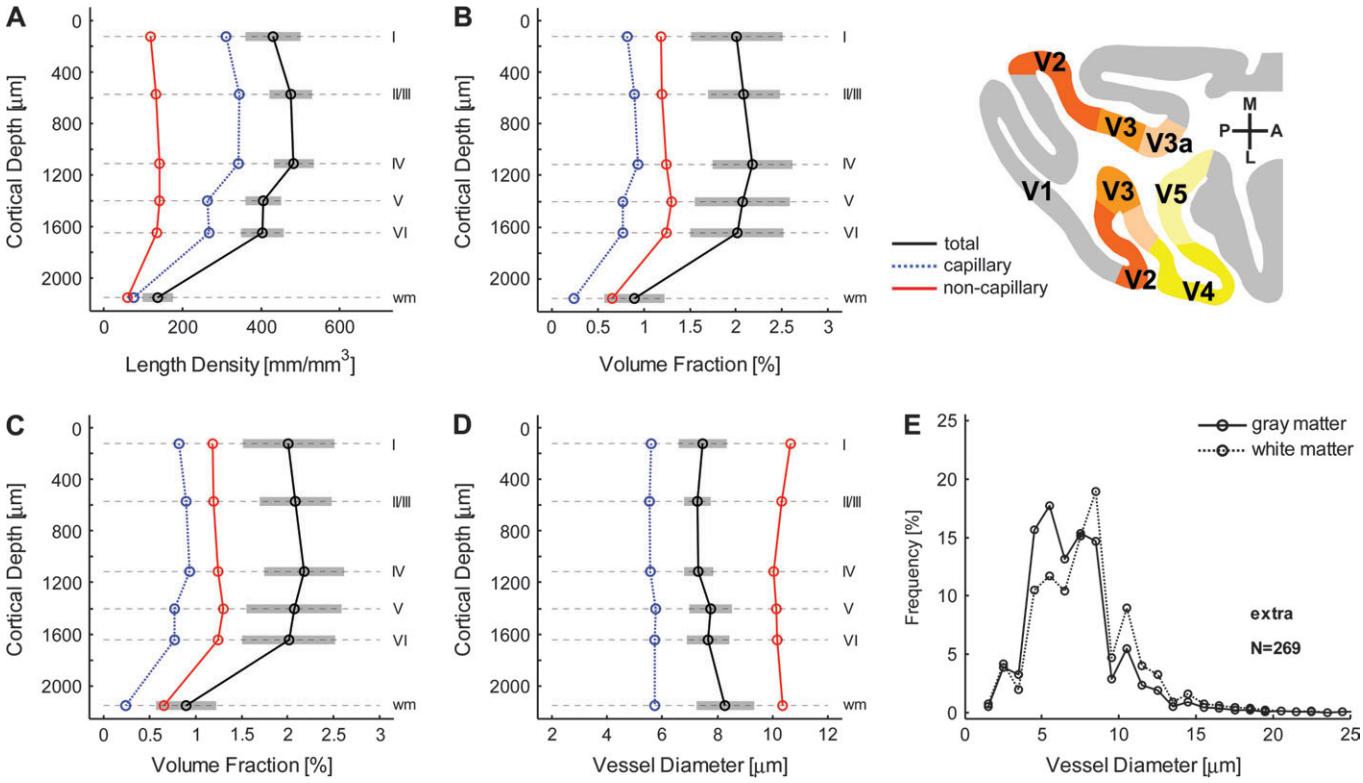

Figure 5. Quantitative values of microvascular system across the cortical layers and cortical depths (µm from cortical surface) in the extrastriate cortex. The black traces show the overall mean density (±standard deviation indicated with gray shaded area). The blue trace shows the values for the capillaries and the red for the noncapillary vessels. (A) Length density in mm/mm^3. (B) Surface density in mm^2/mm^3. (C) Volume fraction in percent. (D) Average vessel diameters in µm. (E) Frequency distribution of vessel calibers for gray and white matter.

structures can be found near the cortical surface and near arterial branching points. Circular constrictions from sphincter-like structures could not be identified with confidence. In very rare cases, a local and sudden decrease in the lumen could be detected; however, it was difficult to differentiate this with confidence from a locally incomplete filling.

Histochemistry

Using digital image processing and stereological analyses of the double histochemically stained sections (Fig. 3), we were able to derive several quantitative measures of the vascular system, including the length density (mm/mm^3), volume fraction (%), surface density (mm^2/mm^3), and mean vessel diameter (µm). A summary of the analysis is shown in Table 1. A total of 459 cortical samples were analyzed throughout the visual cortex (V1 n = 188; V2 n = 78; V3 n = 106; V4 n = 53; V5 n = 34). The mean vascular length density of gray matter in the visual cortex (n = 459) was 478.27 mm/mm^3, whereas the mean volume fraction was 2.14%, and the surface density was 10.97 mm^2/mm^3.

Layer-Specific Analysis of Vascular Density

Significant differences in vascular density measures (length density, volume fraction, and surface density) across cortical layers were observed in all areas investigated (ANOVAs for repeated measures: length density $F_{4/451}$ = 327.7, P < 0.001; volume fraction $F_{4/451}$ = 44.8, P < 0.001; surface density $F_{4/451}$ = 116.2, P < 0.001).

In V1, the vascular density was highest in layer IVc-β (Fig. 4, *A*: volume fraction 2.70%; *B*: length density 627.83 mm/mm^3; *C*: surface density 14.09 mm^2/mm^3). The lowest vascular length and surface density was found in layer I (*B*: length density 408.44 mm/mm^3; *C*: surface density 9.76 mm^2/mm^3), whereas layer 2 showed the lowest volume fraction (*A*: volume fraction 1.93%). Pairwise comparisons of the length densities between layers in V1 revealed significant differences (P < 0.05, Bonferroni-corrected for multiple comparisons) between all layers except between layer IVa and IVb. A summary of the pairwise comparisons between layers in V1 is given in Table 2.

In extrastriate cortex (pooled data V2, V3, V4, and V5, n = 271), layer IV showed the highest vascular density (Fig. 5, *A*: volume fraction 2.18%; *B*: length density 482.98 mm/mm^3; *C*: surface density 11.11 mm^2/mm^3) and layer VI the lowest (Fig. 5, *A*: volume fraction 2.01%; *B*: length density 403.71 mm/mm^3; *C*: surface density 9.74 mm^2/mm^3). Pairwise comparisons of the length density revealed significant differences (P < 0.05, Bonferroni-corrected for multiple comparisons) between all the layers. Similarly, in terms of volume fraction most of the layers were significantly different from each other, except for layers I and V, layers I and VI, and layers II/III and V. A summary of these pairwise comparisons is given in Table 3.

Analysis of Vessel Diameter

In V1 and in the extrastriate cortex, the mean diameter (see Figs 4*D* and 5*D*) differed across the cortical layers ($F_{4/451}$ = 62.6, P < 0.001, pooled data V1–V5). The overall mean diameter was 7.30 µm; the largest diameter (7.66 µm) was found in layer V and the smallest in layer IV (7.18 µm).

The frequency distributions of the vessel calibers for gray and white matter are given in Figures 4*E* and 5*E*. The small

Table 1
Area-specific quantification of microvascular system

	Length density (mm/mm^3)			Surface density (mm^2/mm^3)			Volume fraction (%)			Diameter (μm)		
	Total	Cap	Noncap	Total	Cap	Noncap	Total	Cap	Noncap	Total	Cap	Noncap
V1	512.03 (40.08)	373.92	138.11	11.50 (1.11)	6.80	4.70	2.22 (0.32)	0.97	1.24	7.15 (0.44)	5.43	10.16
V2	453.30 (43.28)	323.95	129.35	10.45 (1.40)	6.02	4.43	2.06 (0.42)	0.87	1.19	7.32 (0.52)	5.56	10.26
V3	460.56 (35.70)	324.95	135.61	10.78 (1.20)	6.08	4.70	2.11 (0.37)	0.86	1.25	7.44 (0.45)	5.59	10.37
V4	437.82 (38.06)	303.61	134.20	10.25 (1.12)	5.70	4.55	2.03 (0.34)	0.83	1.20	7.45 (0.44)	5.61	10.16
V5	467.15 (62.20)	322.95	144.19	10.91 (1.75)	6.00	4.92	2.14 (0.42)	0.85	1.29	7.42 (0.44)	5.56	10.22

Note: The overall mean (total) is shown with standard deviation in brackets as well as the corresponding contribution of capillaries (cap) and noncapillaries (noncap).

caliber vessels, particularly the capillaries with a diameter around 5 μm are clearly the most frequent vessels. A shift toward larger vessels with a considerable drop in capillary frequency can be seen in white matter.

Area-Specific Analysis of Vascular Density

When comparing the vascular density across the areas of the visual cortex, V1 was found to reach the highest levels of vascularization (see Table 1). Pairwise comparisons between V1 and all the other visual subareas revealed a significantly higher length density in V1 (univariate ANOVA, Tukey post hoc tests, $P < 0.05$). No significant differences were found within the extrastriate visual areas except for V4, which showed a slightly lower length density than all other areas (univariate ANOVA, Tukey post hoc tests, $P < 0.05$). The volume fraction was also highest in V1, however, the differences failed to reach significance in the comparisons between V1 versus V3 and V1 versus V5 (univariate ANOVA, Tukey post hoc tests, $P < 0.05$). There was no difference in volume fraction within the extrastriate areas. Similar results were obtained for the surface density, where the density was significantly higher than in all the extrastriate areas except for V5. Again, no difference was detected within the extrastriate areas. The mean vessel diameter was significantly smaller in V1 than in all other visual areas, and no significant differences were found within these extrastriate regions (univariate ANOVA, Tukey post hoc tests, $P < 0.05$).

When comparing individual layers between the visual areas, it was found that the length density of layer IV and layer VI in V1 was significantly higher than in all the extrastriate cortices (univariate ANOVA, Tukey post hoc tests, $P < 0.05$). This was also true for the volume fraction and surface density, however, the comparisons betweens V1 and V5 failed to reach significance for these measures.

Contribution of Capillaries and Noncapillaries

As demonstrated in Figures 4 and 5, the capillaries contribute differentially to the different vascular density quantities. When focusing on the mere length as in length density, it is obvious that by far the largest contribution is provided by the capillaries. However, for other quantities the contribution of the noncapillaries may be higher, according to their respective dependence on the vessel radius (the length density's dependence on the vessel diameter is d^0, that of the surface density is d^1 and that of the volume fraction is d^2). Due to the volume fraction's quadratic dependence on the diameter, the contribution of large vessels surpasses that of the capillaries, despite their much lower frequency. It is important to note that the threshold for the differentiation between capillaries and noncapillaries has a large impact on these measures (details are given in the Appendix and in the Supplementary Fig. 1).

COX Activity

A total of 89 cortical samples from V1 were analyzed. The COX staining shows the well-known characteristic laminar pattern in V1 (Fig. 6). The laminar profile of the semiquantitative COX activity can be seen in Figure 4; it is very obvious that it strictly follows the vascular density. The correlation between vascular density and COX activity proved to be significant, particularly for the capillary vascular density measures (Fig. 6). The correlation coefficients between the vascular density and COX activity across layers were found to be around 0.9 for capillary density (see Fig. 6).

Cell Density

The DAPI images yielded a relative measure of cell density. The layer-specific correlation between cell density and vascular density in V1 revealed a weak relationship in the upper cortical layers. In deeper layers the 2 densities are clearly more closely correlated (Fig. 6 and Supplementary Fig. 2). When all the layers are considered, only the correlation between the capillary length and surface density and the cell density proved to be significant.

Discussion

Qualitative Aspects as Assessed by the Corrosion Cast Technique

To our knowledge, this is the 1st study applying the corrosion cast technique to investigate the cerebral vasculature in the macaque monkey. As expected, the general organization of the cerebral vasculature is very similar to that described for other species (e.g., the human Duvernoy et al. 1981; Reina-De La Torre et al. 1998).

We were able to detect abundant perivascular structures. These ring-like structures were only found around arteries, and were most frequently located near the surface of the cortex or before or after arterial branching points. Although the origin of these structures is still debated (Castenholz et al. 1982; Aharinejad et al. 1990; Rodriguez-Baeza et al. 1998), we favor the hypothesis that they originate from resin being pushed into space normally occupied by arterial smooth muscles. A reason for this could be that in the process of perfusion, fixation, and/or resin injection, the tight junctions at the endothelial cells are ruptured at certain locations. Circular constrictions from sphincter-like structures, as described by others (Rodriguez-Baeza et al. 1998; Harrison et al. 2002), could not be detected in our samples. It is important to note that these constrictions should also be visible in the basal membrane, that is, in the anticollagen stain. Taken together, using both immunostaining of the basal membrane as well as corrosion casts, we were

Table 2
Laminar differences in V1

Length Density [Δ in %]

	I	II	III	IVa	IVb	IVca	IVcb	V	VI
I		10.8	17.1	28.8	27.4	47.6	53.7	6.1	20.8
II			5.7	16.3	15.0	33.3	38.7	-4.2	9.0
III				10.0	8.8	26.0	31.2	-9.4	3.1
IVa					-1.1	14.6	19.3	-17.6	-6.3
IVb						15.9	20.6	-16.7	-5.2
IVca							4.1	-28.1	-18.2
IVcb								-30.9	-21.4
V									13.8
VI									

Volume Fraction [Δ in %]

	I	II	III	IVa	IVb	IVca	IVcb	V	VI
I		-5.4	-2.2	4.3	6.2	26.1	32.4	2.1	15.5
II			3.4	10.3	12.3	33.4	40.0	7.9	22.1
III				6.6	8.6	29.0	35.4	4.4	18.0
IVa					1.9	20.9	27.0	-2.1	10.7
IVb						18.7	24.7	-3.9	8.7
IVca							5.0	-19.1	-8.5
IVcb								-22.9	-12.8
V									13.1
VI									

Surface Density [Δ in %]

	I	II	III	IVa	IVb	IVca	IVcb	V	VI
I		3.8	8.5	16.1	15.8	36.7	44.3	4.9	20.6
II			4.4	11.8	11.5	31.7	38.9	1.1	16.1
III				7.1	6.8	26.1	33.0	-3.2	11.2
IVa					-0.3	17.7	24.2	-9.6	3.8
IVb						18.1	24.6	-9.4	4.1
IVca							5.5	-23.2	-11.8
IVcb								-27.3	-16.4
V									14.9
VI									

Note: Laminar differences in length density, volume fraction, and surface density. The differences between 2 laminae are shown in percent. Gray shaded areas indicate differences that did *not* reach statistical significance.

Table 3
Laminar differences in extrastriate cortex

Length Density [Δ in %]

	I	II/III	IV	V	VI
I		10.6	12.4	-5.9	-5.9
II/III			1.6	-14.9	-15.0
IV				-16.3	-16.3
V					-0.1
VI					

Volume Fraction [Δ in %]

	I	II/III	IV	V	VI
I		4.0	8.7	3.3	0.3
II/III			4.5	-0.7	-3.5
IV				-5.0	-7.7
V					-2.9
VI					

Surface Density [Δ in %]

	I	II/III	IV	V	VI
I		8.1	10.5	-1.9	-3.2
II/III			2.1	-9.3	-10.5
IV				-11.2	-12.3
V					-1.3
VI					

Note: Laminar differences in length density, volume fraction, and surface density. The differences between 2 laminae are shown in percent. Gray shaded areas indicate differences that did *not* reach statistical significance.

unable to detect a relevant number of constrictions. It is obvious that the presence or absence of such constrictions depends on the tone of the smooth muscles and pericytes surrounding the vessel and that this muscle tone is substantially influenced by the perfusion and fixation procedure. Therefore, it might be that these constrictions do exist in vivo, most likely in a constricted state by default in order to allow the increase of blood flow on demand, but that they are dilated in the course of perfusion and fixation.

Unlike others (Harrison et al. 2002), we were unable to detect apparent discontinuities in the vasculature. Instead, we found a homogeneously distributed vasculature along both the tangential and the in-depth direction of cortex. This is also what one would expect, because the intercapillary mesh size is most likely determined by the diffusion coefficient of oxygen, which is approximately 50 μm in gray matter. A discontinuous

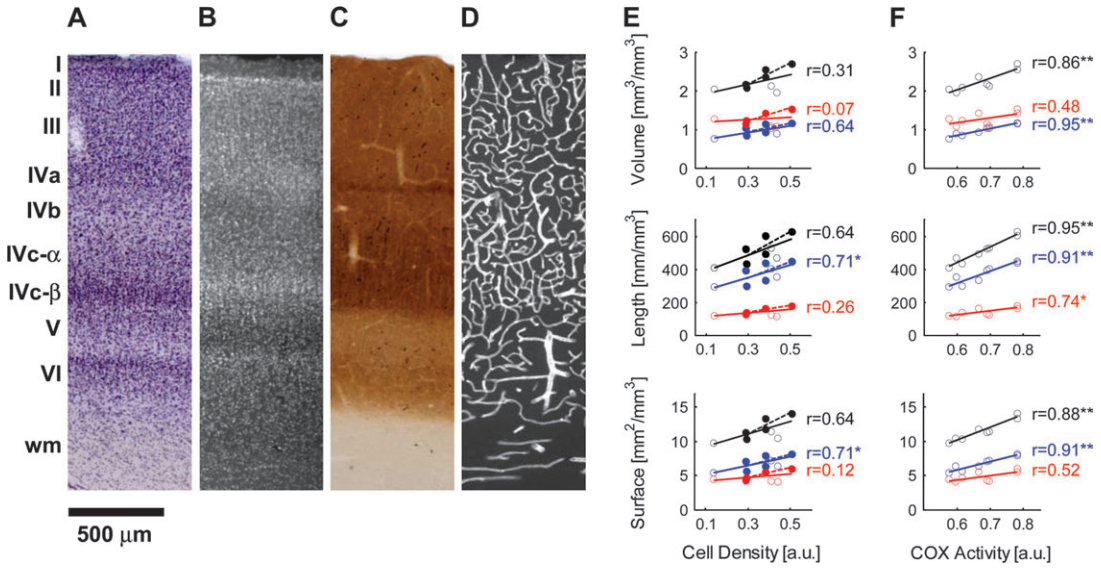

Figure 6. COX activity and cell density in V1. Representative Nissl (*A*), DAPI (*B*), COX (*C*), and anticollagen stain (*D*) of V1 section showing the characteristic laminar pattern of the area. The relationship between cell density and vascular density is shown in (*E*). In the lower cortical layers (layers IV, V, and VI; represented by solid circles and dashed regression line) the correlation is stronger than in the upper layers (layers I, II and III; represented by open circles). The level of basal oxidative metabolism as measured by COX activity staining correlates well with the vascular density measures (*F*). The data represent the mean values from all layer-specific ROIs for the vascular density (*y*-axis) and COX activity (*x*-axis). The vascular data and the COX data were measured in different animals. The blue values represent the capillary and the red represent the noncapillary density, whereas the black traces are based on the total vascular density. The Spearman rank correlation coefficient is provided with its corresponding level of statistical significance (**$P<0.001$, *$P<0.01$).

vascular system as proposed by Harrison et al. (2002) would therefore probably fail to meet the high steady-state metabolic demand of the cortex. We believe that the main reason for the proposed discontinuity of the vasculature was an incomplete intravascular filling. Round or tapered dead ends are well-known indicators of incomplete intravascular filling (for an excellent review on the vascular corrosion cast method, see Lametschwandtner et al. 1990). One could argue that the incomplete filling is due to "physiologically" closed vessels, as suggested by the controversial capillary recruitment phenomenon (Gobel et al. 1989; Pinard et al. 2000). However, in the work of Harrison and colleagues many dead ends can be seen in large vessels for which a recruitment mechanism has never been proposed and can therefore be ruled out.

In spite of their undisputed usefulness for the *qualitative* assessment of the vasculature with great detail (e.g., differentiation between arteries and veins, demonstration of perivascular structures) reliable *quantitative* volumetric data from corrosion casts are difficult to acquire. It is important to note that the technical difficulties become even more pronounced in larger animals such as the macaque monkey. Another disadvantage of the corrosion cast technique is that the tissue is lost due to the maceration process, which renders an exact localization within or between areas impossible. Therefore, we chose to supplement it with a histological approach for an exact layer- and area-specific quantification of the vasculature in the macaque visual cortex.

Quantitative Aspects as Assessed by Immunohistochemistry

One can assume that the density of the vascular network is optimized for a number of parameters. For example, the network has to be dense enough to make sure that diffusion of oxygen and transport of energy substrates are in register with the enormous metabolic activity of brain tissue. On the other hand, the network has to be sparse enough to comply with space and cost limitations. To our knowledge, this is the 1st quantitative study of the macaque cerebral microvasculature (quantitative in the strict sense, i.e., providing density values with units such as mm/mm^3). The vascular density values were stereologically determined on the basis of anticollagen immunohistochemistry from a large number of samples. Although the absolute values have to be treated with a certain amount of caution (see methodological remarks), they are well within the range of earlier studies performed in other species and using different methods. The overall vascular length density in visual gray matter lies around 478 mm/mm^3, whereas the volume fraction is approximately 2.1%.

It is important to note that the computed density variables (length density, surface, and volume fraction) are not strictly independent. They depend differently on the mean vascular diameter of a given region (consult the Appendix for a more comprehensive consideration of this issue). At any rate, because all 3 variables have distinct physiological implications it seemed appropriate to present each of them separately.

Area-Specific Vascular Density

It has been described before that the primary visual cortex seems to be unique with respect to the microvascular system as well (Zheng et al. 1991; Fonta and Imbert 2002; Tieman et al. 2004). Overall vascular density is clearly higher in the striate cortex than in the extrastriate cortices. One novel finding of the present study was the fact that the differences within the several extrastriate areas were small or even negligible. Interestingly, the difference between the primary and non-primary areas was also found in the somatosensory and auditory cortex (data not shown), and again, the vascular densities of the secondary auditory and somatosensory areas were comparable with those of the extrastriate cortex. A detailed quantitative description of the nonvisual areas would clearly be beyond the

scope of the present work and will be presented elsewhere. Taken together, it seems that nonprimary areas share the same microvascular architecture. From a mere structural point of view large differences in the hemodynamic response are not to be expected within these areas. However, our results clearly suggest that caution is advised when hemodynamic response patterns are compared between primary and nonprimary areas.

Layer-Specific Vascular Density

In the primary visual cortex, we found a marked gradient in the microvascular density along the cortical layers, with the highest density in layer IVc-β. This is in agreement with studies in the squirrel monkey (Zheng et al. 1991) and the marmoset (Fonta and Imbert 2002). In a semiquantitative study, Fonta and Imbert (2002) were able to demonstrate that the relative vascular density developed in parallel to COX activity and was highest in layer IVc-α in the 1st postnatal month. Shortly afterward the 2 layers match in vascular density and COX activity, before layer IVc-β eventually becomes the most densely vascularized layer. In the cat, a similar change in steady-state metabolic demand and vascular density was observed. It was found that layer IV in the cat striate area 17 showed the highest relative vascular density and relative glucose utilization. However, this laminar difference could only be found in the adult but not in 5-week-old kittens (Tieman et al. 2004).

As shown in other species the extrastriate cortex exhibits a lower vascular density than the primary visual area (Duvernoy et al. 1981; Zheng et al. 1991; Tieman et al. 2004) and the laminar differences are clearly less pronounced, a result that is also seen when comparing laminar differences in cell and synapse densities. Furthermore, the laminar differences are very similar within the subareas of the extrastriate cortex.

Length Density versus Volume Fraction

It is interesting to note that in general, differences in length density were more pronounced than differences in volume fraction (be it between layers or areas). As an example, V1 has an overall length density that is 11% higher than in V2, whereas the difference in volume fraction is only 7%. Moreover, the mean diameter of the vessels is somewhat lower in V1 than in V2. Taken together, these results indicate that the capillary rather than the overall vascular density is increased in order to match the needed supply of oxygen and energy substrates. In principle there are 2 ways to increase capillary density, namely capillary proliferation and capillary segment elongation (Mironov et al. 1994). However, to differentiate these 2 mechanisms, 3-dimensional data acquisition is mandatory, for example, using either confocal microscopy (Cassot et al. 2006) or synchrotron-radiation based x-ray microscopy (srXTM) (Plouraboue et al. 2004; Heinzer et al. 2006). Our own preliminary data obtained from srXTM clearly indicate a greater contribution of an increased number of capillaries as opposed to an increase in capillary segment length or tortuosity (data not shown). In hypobaric hypoxia, it was shown that the opposite is the case, indicating that in acute situations the brain reacts with capillary segment elongation (Mironov et al. 1994).

Methodological Issues

The anticollagen staining and subsequent image processing proved to be an adequate approach that provides density measures that are within the range of previously published data from other species and/or cortical areas. However, there are certain methodological issues that need to be addressed. First, the overall volume fraction is lower than that derived from other methods, such as positron emission tomography using CO inhalation. One of the reasons for this could be that the large pial vessels (see corrosion cast images in Fig. 1) are not included in our immunohistochemical data. Furthermore, some large vessels are lost during the processing of the sections. Although the large vessels are scarce, they contribute considerably to the vascular volume, as elaborated above. The segmentation process that eventually yields the binarized vessel data, of course, considerably influences the quantified vascular density values. Although great care was taken to optimize this process, one has to be aware that some error is to be expected, as in most fully quantitative studies. Our preliminary data using synchrotron-based X-ray microscopy confirm the density values presented in this study. Future work will profit considerably from this new technology, because it can produce true volumetric data from a large field of view with sufficient resolution. Tomographic methods will be the basis of required investigations of the vascular network topology in physiology and pathology.

One of the major drawbacks of the applied immunohistochemical method is the inability to differentiate between arterial and venous vessels, which was possible using the corrosion cast technique. There are several studies that suggest specific antibodies for either arteries or veins, at least in the developing and unfixed brain tissue (e.g., smooth muscle actin, eph, ephrin). We have screened these antibodies but we were unable to produce satisfying results in the adult well-fixed macaque brain.

Vascular Density: Correlation with Element Density or Regional Metabolic Activity?

An important issue concerns the covariation of vascular density with the density of neurons, synapses and glia. The fact that perisynaptic elements are the most costly in terms of energy metabolism (Mata et al. 1980; Erecinska and Dagani 1990; Jueptner and Weiller 1995) would argue in favor of a tighter relationship between vascular density and the synaptic rather than the neuronal density (Logothetis and Wandell 2004). Interestingly, the data we present here show that this assumption is wrong. In fact, correlating the layer-specific densities of neurons, synapses, and glia from the literature (O'Kusky and Colonnier 1982; Bourgeois and Rakic 1993) with the vascular density of the present data suggests that the correlation between the synaptic and vascular density is very weak (see Supplementary Fig. 3), particularly because layers II and III show a high synaptic but rather low vascular density. For the upper cortical layers, the correlation between our semi-quantitative cell density measure and the vascular density proved to be rather weak. Furthermore, neuronal density measures taken from the literature (O'Kusky and Colonnier 1982; Bourgeois and Rakic 1993) did not correlate significantly with the vascular density assessed in the present study. Taken together, these facts indicate that there is a weak positive correlation between cellular (particularly neuronal) density and vascular density. However, when focusing on layer I, it becomes obvious that these relationships are not straightforward. As described by others, layer I exhibits an extremely low neuronal density, and there the vascular density is clearly more closely related to the synaptic density (Duvernoy et al. 1981). The comparison between the vascular data and the values for

the cellular (own data and from literature) and synaptic density (from literature) provide an adequate 1st approximation of this important relationship. Measuring the synaptic and cellular densities in identical samples is a mandatory next step, although our existing data together with the observation briefly discussed in the next paragraph suggest that element density and vascular density need not necessarily be strongly correlated in a system optimizing the coupling of steady-state neuronal activity with its supply of energy.

In particular, to better understand the underlying reasons for vascular density distribution, we used an established methodology (COX) to measure the regional energy consumption in the same cortical areas of different animals. In contrast to the weak correlations with synaptic density and cellular densities (in upper cortical layers) we found a tight relationship between metabolic demand and vascular density. Correlations between the layer-specific COX activity and the capillary density measures were very strong in V1. This is in agreement with earlier studies, although most of them did not investigate the relationship in a strictly quantitative way (Zheng et al. 1991; Cox et al. 1993; Riddle et al. 1993; Woolsey et al. 1996; Fonta and Imbert 2002; Tieman et al. 2004). Techniques such as the 2-deoxyglucose method would be more effective for quantitatively assessing the metabolic rate. Yet, the remarkable relationship between the measured vascular density and the semiquantitative COX activities indicates that the use of the method in this study is justified, at least as a 1st approximation.

Strictly speaking, the fact that the vascular density correlates well with the steady-state metabolic demand is hardly surprising. What is interesting, and perhaps unexpected, is rather the dissociation of energy demand and element density in cortex. We speculate that this dissociation reflects the degree of differentiated integration of a cortical area. A typical pyramidal cell in the primate cortex receives approximately 10 000 inputs, and a column underneath 1 mm^2 in the visual cortex has approximately 200 000 neurons (Braitenberg and Schuez 1998). Given the weak thalamic input in any cortical area (approximately 10–15% of the area's total input), these very large numbers suggest a context-dependent integration of information, according to which regional processing probably never reflects the activation of all synapses and cells at any given time in life. Instead, the steady-state energy demands follow the default functional mode of the system, which might in turn echo the average feedforward input to an area together with the average neuromodulatory effects of the ascending diffuse systems. Effects related to cognitive states or to different types of sensory–motor integrative actions may be entirely context-dependent and not co-occurring; in other words the number of regional elements might never be recruited at the same time. If so, element density reflects a region's capacity to process information, whereas vascular density and energy consumption reflect the minimal processes that are instantiated in the region's idling state. Finally, the explanation of the fact that the laminae IV–VI displayed a much closer relationship between cell density and vascular density than the upper layers is subject to future research, which will have to include data of cell type–specific densities.

Implications for Functional Imaging Based on Hemodynamic Responses

It is evident that the understanding of the signals originating from noninvasive functional neuroimaging modalities such as functional magnetic resonance imaging in part relies on a profound knowledge of the cerebrovascular structure (Turner 2002). The quantitative analysis of the area- and layer-specific vascular density is a 1st important step and will provide important information for theoretical considerations that in part rely on such values. For example, many models of the BOLD signal require the blood volume fraction as an a priori parameter (Buxton et al. 1998, 2004) and it has so far been disregarded that differences might exist within or between cortical areas. One ultimate goal would be to estimate a vascular point spread function (Logothetis and Wandell 2004; Weber et al. 2004; Sheth, Nemoto, Guiou, Walker, Pouratian, Hageman, et al. 2004; Dunn et al. 2005; Sheth et al. 2005) on the basis of the vascular structure. To achieve this, the density of the blood-flow-regulating structures has to be known. This would—above all—involve the differentiation of arteries from veins, because the smooth muscle sheath around the arteries is a key player in regulating the vascular resistance. Furthermore, the density of all other contractile elements, such as sphincter-like perivascular structures (Rodriguez-Baeza et al. 1998) or pericytes (Peppiatt et al. 2006) has to be assessed. The corrosion cast data provide clear evidence that the draining volume of large penetrating cortical veins is considerably larger than the feeding territory of a penetrating cortical artery. It was recently shown that these arteries can be considered a bottleneck in the feeding system, because photothrombosis of individual vessels of this type leads to a severe disruption of perfusion in an area extending as far as 350 μm in radius (Nishimura et al. 2007). One of the most frequently used imaging sequences in BOLD fMRI—gradient echo echo-planar imaging (EPI)—is sensitive to local susceptibility gradients, which originate predominantly near draining veins. On the basis of the present data, the ultimate spatial resolution of an imaging scheme based on the penetrating venous vessels would be around 0.70 mm^3. It is evident that imaging signals originating from arteries (feeding volume 0.44 mm^3) or even better from capillaries—such as spin-echo EPI—would provide a superior spatial resolution (Lee et al. 1999; Yacoub et al. 2003; Goense and Logothetis 2006; Harel et al. 2006; Goense et al. 2007).

A better and more quantitative understanding of cerebral blood flow control could be obtained through fluid dynamic modeling. For this purpose, *tomographic* assessments of the vasculature in large cortical fields of view are necessary to obtain the 3-dimensional topology of the vascular network, using the currently available methods mentioned above (Plouraboue et al. 2004; Cassot et al. 2006; Heinzer et al. 2006).

The fact that the microvascular system of the primary visual cortex (and also the primary somatosensory and auditory cortices) is clearly different from the nonprimary regions has direct and important implications for functional neuroimaging studies. Although the influence of vascular density on the hemodynamic response is a subject for further research, caution is advised in studies that draw conclusions from differential signals measured in primary versus nonprimary cortical areas. It might be argued that a higher microvascular density causes an increased signal-to-noise ratio of the hemodynamic signals and consequently increases the chances of detecting differences between conditions.

Supplementary Material

Supplementary material can be found at: http://www.cercor.oxfordjournals.org/.

Funding

Max Planck Society; Schweizerische Stiftung für biologisch-medizinische Studien SSMBS; and by the Swiss National Science Foundation (PP00B—110751/1).

Notes

We thank Almut Schüz, Heinz Schwarz, Gregory J. del Zoppo for their help with the immunohistochemical procedures and for important discussions as well as Denis Chaimow for stereological suggestions.

Conflict of Interest: None declared.

Address correspondence to Bruno Weber, Institute of Pharmacology and Toxicology, University of Zürich, Rämistrasse 100, 8091 Zürich and Nikos Logothetis, Max Planck Institute für biologische Kybernetik, Spemannstr. 38, 72076 Tübingen, Germany.

Appendix

As illustrated in Figure 3, the raw anticollagen images can be thresholded and binarized, yielding an area fraction A_F. The parameters for the image processing were kept constant for all samples. It is obvious that the choice of the threshold significantly influences the resulting A_F. The parameters were carefully set in order to optimize the match between the raw image (Fig. 3*E*) and the binarized image (Fig. 3*F*). This optimization was guided by visual inspection. By eroding the binarized images to single lines, we were able to produce the eroded area fraction E_F (Fig. 3*G*). From A_F, E_F and the remaining known quantities (pixel width a_{pix} and slice thickness t), the length density L_V, the surface density S_V, and volume fraction V_V of the blood vessels can be derived.

Area Fraction

The area fraction A_F is defined as the quotient of the total projected vessel area and the total area of the projection A_{total}. If we approximate the vascular tree by a network of cylinders i with lengths l_i and diameters d_i, we can write

$$A_F = \frac{\sum_i l_{pi} d_i}{A_{total}} = \frac{\sum_i f_i l_i d_i}{A_{total}} = f \frac{\sum_i l_i d_i}{A_{total}} \quad (1)$$

Here, f_i is the ratio of projected and true vessel lengths. In the last step it was assumed that this factor is uniform across all vessels.

As the projection image is not continuous, but consists of pixel elements, the projected area in the pixel image A_F^{pix} will differ from the true projected area by a factor p_A.

Thus,

$$A_F^{pix} = A_F p_A = f p_A \frac{\sum_i l_i d_i}{A_{total}} = f p_A \frac{\sum_i l_i d_i}{N_{pix} a_{pix}^2}, \quad (2)$$

where N_{pix} denotes the total number of pixels in the projection image. The lengths l_i in the pixel image are multiples of the pixel-length a_{pix}.

Eroded Area Fraction

Analogous to A_F, the eroded area fraction E_F can be calculated by

$$E_F = \frac{\sum_i l_{pi} d_u}{A_{total}} = \frac{\sum_i f_i l_i d_u}{A_{total}} = f d_u \frac{\sum_i l_i}{A_{total}} \quad (3)$$

where d_u is the unit diameter.

The pixel image will introduce an additional factor p_E, yielding

$$E_F^{pix} = E_F p_E = f d_u p_E \frac{\sum_i l_i}{A_{total}} = f a_{pix} p_E \frac{\sum_i l_i}{N_{pix} a_{pix}^2} \quad (4)$$

Equations (1–4) do not take into account crossings of blood vessels in the projection image and therefore the present study slightly underestimates the projected length.

Length Density

The length density L_V of the blood vessels in the volume V_{total} is given by

$$L_V = \frac{\sum_i l_i}{V_{total}} = \frac{E_F A_{total}}{f d_u V_{total}} = \frac{E_F}{f d_u t} = \frac{4 E_F}{\pi d_u t} \quad (5)$$

In the last step an isotropic orientation of the vessels was assumed, resulting in $f = \pi/4$ (see also Russ and Dehoff 2000). The length density in the pixel image can thus be expressed as

$$L_V = \frac{4 E_F^{pix}}{\pi a_{pix} t p_E} \quad (6)$$

Surface Density

Just as the length density can be expressed in terms of the eroded area fraction, the area fraction can be used to calculate the surface density S_V.

$$S_V = \frac{\sum_i l_i \pi d_i}{V_{total}} = \frac{\pi A_F A_{total}}{f V_{total}} = \frac{\pi A_F}{f t} = \frac{4 A_F}{t} \quad (7)$$

The pixel image relates to S_V in the following way

$$S_V = \frac{4 A_F^{pix}}{t \quad p_A}. \quad (8)$$

Volume Fraction

The volume fraction V_F can be written as

$$V_F = \frac{\sum_i \pi \left(\frac{d_i}{2}\right)^2 l_i}{V_{total}} = \frac{\pi}{4 V_{total}} \sum_i d_i^2 l_i = \frac{\pi}{4 V_{total}} d_V \sum_i d_i l_i = \frac{S_V}{4} d_V = \frac{d_V A_F}{t}, \quad (9)$$

where d_V denotes a mean diameter. If we assume that $d_V = d_u A_F / E_F$, equation (9) becomes

$$V_F = \frac{d_u A_F^2}{t E_F}. \quad (10)$$

For a pixel image, the above relation will change to

$$V_F = a_{pix} \frac{\left(A_F^{pix}\right)^2 p_E}{t E_F^{pix} \quad p_A^2}. \quad (11)$$

Threshold Dependence of Capillary Contribution to Vascular Density

In addition to the overall quantification, we analyzed the data separately for capillaries and the remaining larger vessels (noncapillaries). Because capillaries cannot be differentiated qualitatively from other vessel types on the anticollagen stains, this differentiation had to be based on the caliber. We chose a threshold of 8 μm. It is obvious that the choice of this threshold greatly influences the relative contributions of capillaries and noncapillaries. To demonstrate this dependence, we computed the capillary and noncapillary length density, surface density and volume density, applying a range of thresholds. In Supplement Figure 1, capillary and noncapillary density measures are shown as a function of the threshold. It can easily be seen that the crossing of the capillary and noncapillary traces (i.e., equal contribution of the 2 vessel classes) shifts to the right with increasing dependence on the diameter (d^0 for length density, d^1 for surface density, d^2 for volume fraction).

References

Aharinejad S, Lametschwandtner A, Holtl W, Firbas W. 1990. The microvasculature of the guinea pig ureter. A scanning electron microscopic investigation. Scanning Microsc. 4:957–965; discussion 965–956.

Bourgeois JP, Rakic P. 1993. Changes of synaptic density in the primary visual cortex of the macaque monkey from fetal to adult stage. J Neurosci. 13:2801–2820.

Braitenberg V, Schuez A. 1998. Cortex, statistic and geometry of neuronal connectivity. Berlin: Springer.

Buxton RB, Uludag K, Dubowitz DJ, Liu TT. 2004. Modeling the hemodynamic response to brain activation. Neuroimage. 23(Suppl 1): S220–S233.

Buxton RB, Wong EC, Frank LR. 1998. Dynamics of blood flow and oxygenation changes during brain activation: the balloon model. Magn Reson Med. 39:855–864.

Carroll EW, Wong-Riley MT. 1984. Quantitative light and electron microscopic analysis of cytochrome oxidase-rich zones in the striate cortex of the squirrel monkey. J Comp Neurol. 222:1–17.

Cassot F, Lauwers F, Fouard C, Prohaska S, Lauwers-Cances V. 2006. A novel 3-dimensional computer-assisted method for a quantitative study of microvascular networks of the human cerebral cortex. Microcirculation. 13:1–18.

Castenholz A, Zoltzer H, Erhardt H. 1982. Structures imitating myocytes and pericytes in corrosion casts of terminal blood vessels. A methodical approach to the phenomenon of "plastic strips" in SEM. Mikroskopie. 39:95–106.
Cox SB, Woolsey TA, Rovainen CM. 1993. Localized dynamic changes in cortical blood flow with whisker stimulation corresponds to matched vascular and neuronal architecture of rat barrels. J Cereb Blood Flow Metab. 13:899–913.
Devor A, Dunn AK, Andermann ML, Ulbert I, Boas DA, Dale AM. 2003. Coupling of total hemoglobin concentration, oxygenation, and neural activity in rat somatosensory cortex. Neuron. 39:353–359.
Dunn AK, Devor A, Dale AM, Boas DA. 2005. Spatial extent of oxygen metabolism and hemodynamic changes during functional activation of the rat somatosensory cortex. Neuroimage. 27:279–290.
Duvernoy HM, Delon S, Vannson JL. 1981. Cortical blood vessels of the human brain. Brain Res Bull. 7:519–579.
Erecinska M, Dagani F. 1990. Relationships between the neuronal sodium/potassium pump and energy metabolism. Effects of K+, Na+, and adenosine triphosphate in isolated brain synaptosomes. J Gen Physiol. 95:591–616.
Fonta C, Imbert M. 2002. Vascularization in the primate visual cortex during development. Cereb Cortex. 12:199–211.
Fukuda S, Fini CA, Mabuchi T, Koziol JA, Eggleston LL, Jr, del Zoppo GJ. 2004. Focal cerebral ischemia induces active proteases that degrade microvascular matrix. Stroke. 35:998–1004.
Gobel U, Klein B, Schrock H, Kuschinsky W. 1989. Lack of capillary recruitment in the brains of awake rats during hypercapnia. J Cereb Blood Flow Metab. 9:491–499.
Goense JB, Logothetis NK. 2006. Laminar specificity in monkey V1 using high-resolution SE-fMRI. Magn Reson Imaging. 24:381–392.
Goense JB, Zappe AC, Logothetis NK. 2007. High-resolution fMRI of macaque V1. Magn Reson Imaging. 25:740–747.
Hamann GF, Okada Y, Fitridge R, del Zoppo GJ. 1995. Microvascular basal lamina antigens disappear during cerebral ischemia and reperfusion. Stroke. 26:2120–2126.
Harel N, Lin J, Moeller S, Ugurbil K, Yacoub E. 2006. Combined imaging-histological study of cortical laminar specificity of fMRI signals. Neuroimage. 29:879–887.
Harrison RV, Harel N, Panesar J, Mount RJ. 2002. Blood capillary distribution correlates with hemodynamic-based functional imaging in cerebral cortex. Cereb Cortex. 12:225–233.
Heinzer S, Krucker T, Stampanoni M, Abela R, Meyer EP, Schuler A, Schneider P, Muller R. 2006. Hierarchical microimaging for multiscale analysis of large vascular networks. Neuroimage. 32:626–636.
Jones M, Hewson-Stoate N, Martindale J, Redgrave P, Mayhew J. 2004. Nonlinear coupling of neural activity and CBF in rodent barrel cortex. Neuroimage. 22:956–965.
Jueptner M, Weiller C. 1995. Review: does measurement of regional cerebral blood flow reflect synaptic activity? Implications for PET and fMRI. Neuroimage. 2:148–156.
Kwong KK, Belliveau JW, Chesler DA, Goldberg IE, Weisskoff RM, Poncelet BP, Kennedy DN, Hoppel BE, Cohen MS, Turner R, et al. 1992. Dynamic magnetic resonance imaging of human brain activity during primary sensory stimulation. Proc Natl Acad Sci USA. 89:5675–5679.
Lametschwandtner A, Lametschwandtner U, Weiger T. 1990. Scanning electron microscopy of vascular corrosion casts—technique and applications: updated review. Scanning Microsc. 4:889–940; discussion 941.
Lee SP, Silva AC, Ugurbil K, Kim SG. 1999. Diffusion-weighted spin-echo fMRI at 9.4 T: microvascular/tissue contribution to BOLD signal changes. Magn Reson Med. 42:919–928.
Logothetis NK, Pauls J, Augath M, Trinath T, Oeltermann A. 2001. Neurophysiological investigation of the basis of the fMRI signal. Nature. 412:150–157.
Logothetis NK, Wandell BA. 2004. Interpreting the BOLD signal. Annu Rev Physiol. 66:735–769.
Martindale J, Berwick J, Martin C, Kong Y, Zheng Y, Mayhew J. 2005. Long duration stimuli and nonlinearities in the neural-haemodynamic coupling. J Cereb Blood Flow Metab. 25:651–661.
Mata M, Fink DJ, Gainer H, Smith CB, Davidsen L, Savaki H, Schwartz WJ, Sokoloff L. 1980. Activity-dependent energy metabolism in rat posterior pituitary primarily reflects sodium pump activity. J Neurochem. 34:213–215.
Michaloudi H, Grivas I, Batzios C, Chiotelli M, Papadopoulos GC. 2005. Areal and laminar variations in the vascularity of the visual, auditory, and entorhinal cortices of the developing rat brain. Brain Res Dev Brain Res. 155:60–70.
Miodonski A, Hodde K, Bakker C. 1976. Rasterelektronenmikroskopie von Plastik Korrosions Präparaten: morphologische Unterschiede zwischen Arterien und Venen. BEDO. 9:435–442.
Mironov V, Hritz MA, LaManna JC, Hudetz AG, Harik SI. 1994. Architectural alterations in rat cerebral microvessels after hypobaric hypoxia. Brain Res. 660:73–80.
Mosso A. 1881. Ueber den Kreislauf des Blutes im Menschlichen Gehirn. Leipzig: Von Veit.
Nishimura N, Schaffer CB, Friedman B, Lyden PD, Kleinfeld D. 2007. Penetrating arterioles are a bottleneck in the perfusion of neocortex. Proc Natl Acad Sci USA. 104:365–370.
O'Kusky J, Colonnier M. 1982. A laminar analysis of the number of neurons, glia, and synapses in the adult cortex (area 17) of adult macaque monkeys. J Comp Neurol. 210:278–290.
Ogawa S, Lee TM, Kay AR, Tank DW. 1990. Brain magnetic resonance imaging with contrast dependent on blood oxygenation. Proc Natl Acad Sci USA. 87:9868–9872.
Peppiatt CM, Howarth C, Mobbs P, Attwell D. 2006. Bidirectional control of CNS capillary diameter by pericytes. Nature. 443:700–704.
Pinard E, Engrand N, Seylaz J. 2000. Dynamic cerebral microcirculatory changes in transient forebrain ischemia in rats: involvement of type I nitric oxide synthase. J Cereb Blood Flow Metab. 20:1648–1658.
Plouraboue F, Cloetens P, Fonta C, Steyer A, Lauwers F, Marc-Vergnes JP. 2004. X-ray high-resolution vascular network imaging. J Microsc. 215:139–148.
Reina-De La Torre F, Rodriguez-Baeza A, Sahuquillo-Barris J. 1998. Morphological characteristics and distribution pattern of the arterial vessels in human cerebral cortex: a scanning electron microscope study. Anat Rec. 251:87–96.
Riddle DR, Gutierrez G, Zheng D, White LE, Richards A, Purves D. 1993. Differential metabolic and electrical activity in the somatic sensory cortex of juvenile and adult rats. J Neurosci. 13:4193–4213.
Rodriguez-Baeza A, Reina-De La Torre F, Ortega-Sanchez M, Sahuquillo-Barris J. 1998. Perivascular structures in corrosion casts of the human central nervous system: a confocal laser and scanning electron microscope study. Anat Rec. 252:176–184.
Roy CS, Sherrington CS. 1890. On the regulation of the blood supply of the brain. J Physiol. 11:85–108.
Russ J, Dehoff R. 2000. Practical stereology. New York: Plenum Press.
Saleem KS, Logothetis NK. 2006. A combined MRI and histology Atlas of the Rhesus monkey brain. San Diego: Academic Press.
Sheth SA, Nemoto M, Guiou M, Walker M, Pouratian N, Hageman N, Toga AW. 2004. Columnar specificity of microvascular oxygenation and volume responses: implications for functional brain mapping. J Neurosci. 24:634–641.
Sheth SA, Nemoto M, Guiou M, Walker M, Pouratian N, Toga AW. 2004. Linear and nonlinear relationships between neuronal activity, oxygen metabolism, and hemodynamic responses. Neuron. 42:347–355.
Sheth SA, Nemoto M, Guiou MW, Walker MA, Toga AW. 2005. Spatiotemporal evolution of functional hemodynamic changes and their relationship to neuronal activity. J Cereb Blood Flow Metab. 25:830–841.
Stewart PA, Isaacs H, LaManna JC, Harik SI. 1997. Ultrastructural concomitants of hypoxia-induced angiogenesis. Acta Neuropathol (Berl). 93:579–584.
Thomsen K, Offenhauser N, Lauritzen M. 2004. Principal neuron spiking: neither necessary nor sufficient for cerebral blood flow in rat cerebellum. J Physiol. 560:181–189.
Tieman SB, Mollers S, Tieman DG, White J. 2004. The blood supply of the cat's visual cortex and its postnatal development. Brain Res. 998:100–112.

Turner R. 2002. How much cortex can a vein drain? Downstream dilution of activation-related cerebral blood oxygenation changes. Neuroimage. 16:1062–1067.
Vanzetta I, Slovin H, Omer DB, Grinvald A. 2004. Columnar resolution of blood volume and oximetry functional maps in the behaving monkey; implications for FMRI. Neuron. 42: 843–854.
Weber B, Burger C, Wyss MT, von Schulthess GK, Scheffold F, Buck A. 2004. Optical imaging of the spatiotemporal dynamics of cerebral blood flow and oxidative metabolism in the rat barrel cortex. Eur J Neurosci. 20:2664–2670.
Wong-Riley M. 1979. Changes in the visual system of monocularly sutured or enucleated cats demonstrable with cytochrome oxidase histochemistry. Brain Res. 171:11–28.
Wong-Riley MT. 1989. Cytochrome oxidase: an endogenous metabolic marker for neuronal activity. Trends Neurosci. 12:94–101.
Wong-Riley MT, Welt C. 1980. Histochemical changes in cytochrome oxidase of cortical barrels after vibrissal removal in neonatal and adult mice. Proc Natl Acad Sci USA. 77:2333–2337.
Woolsey TA, Rovainen CM, Cox SB, Henegar MH, Liang GE, Liu D, Moskalenko YE, Sui J, Wei L. 1996. Neuronal units linked to microvascular modules in cerebral cortex: response elements for imaging the brain. Cereb Cortex. 6:647–660.
Yacoub E, Duong TQ, Van De Moortele PF, Lindquist M, Adriany G, Kim SG, Ugurbil K, Hu X. 2003. Spin-echo fMRI in humans using high spatial resolutions and high magnetic fields. Magn Reson Med. 49:655–664.
Zheng D, LaMantia AS, Purves D. 1991. Specialized vascularization of the primate visual cortex. J Neurosci. 11:2622–2629.

Publication #2

Behavioral/Systems/Cognitive

Vascularization of Cytochrome Oxidase-Rich Blobs in the Primary Visual Cortex of Squirrel and Macaque Monkeys

Anna Lena Keller,[1] Almut Schüz,[1] Nikos K. Logothetis,[1,2] and Bruno Weber[3]

[1]Max Planck Institute for Biological Cybernetics, 72076 Tübingen, Germany, [2]Imaging Science and Biomedical Engineering, University of Manchester, Manchester M13 9PL, UK, and [3]Institute for Pharmacology and Toxicology, University of Zurich, 8091 Zurich, Switzerland

The close correlation between energy supply by blood vessels and energy consumption by cellular processes in the brain is the basis of blood flow-related functional imaging techniques. Regional differences in vascular density can be detected using high-resolution functional magnetic resonance imaging. Therefore, inhomogeneities in vascularization might help to identify anatomically distinct areas noninvasively *in vivo*. It was reported previously that cytochrome oxidase-rich blobs in the striate cortex of squirrel monkeys are characterized by a notably higher vascular density (42% higher than interblob regions). However, blobs have so far never been identified *in vivo* on the basis of their vascular density. Here, we analyzed blobs of the primary visual cortex of squirrel monkeys and macaques with respect to the relationship between vascularization and cytochrome oxidase activity. By double staining with cytochrome oxidase enzyme histochemistry to define the blobs and collagen type IV immunohistochemistry to quantify the blood vessels, a close correlation between oxidative metabolism and vascularization was confirmed and quantified in detail. The vascular length density in cytochrome oxidase blobs was on average 4.5% higher than in the interblob regions, a difference almost one order of magnitude smaller than previously reported. Thus, the vascular density that is closely associated with local average metabolic activity is a structural equivalent of cerebral metabolism and blood flow. However, the quantitative differences in vascularization between blob and interblob regions are small and below the detectability threshold of the noninvasive hemodynamic imaging methods of today.

Introduction

Cytochrome oxidase (CO) blobs in the primary visual cortex V1 of macaques were described >25 years ago (Horton and Hubel, 1981). Because their functions remain elusive (Sincich and Horton, 2005), noninvasive functional imaging techniques could be a valuable tool for research in this field. Blobs are characterized anatomically as zones of increased CO activity in all cortical layers except IVa and IVc of area V1 (Hendrickson et al., 1981; Horton and Hubel, 1981) and most prominent in lower layer II/III. Blobs have been described for some mammalian species, such as the cat (Murphy et al., 1995), and all primates examined so far [e.g., squirrel monkeys (Fitzpatrick et al., 1983; Carroll and Wong-Riley, 1984), macaques (Horton and Hubel, 1981), and humans (Horton and Hedley-Whyte, 1984; Adams et al., 2007)]. Although there is converging evidence that they are involved in the processing of color, the exact function of blobs remains obscure. Two recent publications (Sincich and Horton, 2005; Lu and Roe, 2008) have provided comprehensive overviews of efforts undertaken so far to clarify this issue. According to these investigators, the conflicting results achieved with methods such as electrophysiology (Livingstone and Hubel, 1988; Ts'O and Gilbert, 1988; Yoshioka and Dow, 1996) and optical imaging (Landisman and Ts'O, 2002) are not necessarily exclusive.

One undisputed fact is the increased oxidative metabolism of the blobs, as shown by CO histochemistry. Such metabolic activity patterns have been linked to certain cortical pathways in primates (Fitzpatrick et al., 1983; Levitt et al., 1995) and correlated with capillary density in rodents (Borowsky and Collins, 1989; Woolsey and Rovainen, 1991). The relationship between vascularization and CO activity has been confirmed by subsequent studies in primates (Zheng et al., 1991; Weber et al., 2008). Specifically, Zheng and colleagues found a difference of 42% in vascular density between blobs and interblobs and also more of the large perpendicular vessels within the blobs in *Saimiri*. Our own recent study found a close correlation between vascularization and laminar organization of CO activity in V1 of macaques (Weber et al., 2008). Layer IVc, with the highest vascular density, was different from the other cortical layers by ~30%, rendering it clearly discernable in high-resolution spin-echo blood oxygenation level-dependent functional magnetic resonance imaging (SE BOLD fMRI) (Goense et al., 2007). Consequently, given the allegedly even higher blob/interblob difference found by Zheng and colleagues and a blob size of ~0.25 mm, blobs should be detectable using high-resolution MRI. However, to our knowledge, blobs have never been identified using MRI technology. This led to the present study, in which a careful reappraisal of CO activity, vascular density, and evaluation of perpendicular vessels was performed in V1 of macaque and squirrel monkey. We did

Received June 1, 2010; revised Nov. 5, 2010; accepted Nov. 7, 2010.

This work was supported by the Max Planck Society and by Swiss National Science Foundation Grant PP0033-110751. We thank Prof. Dr. Ernst Pöppel and the University of Munich for providing us with the monkeys used in this study. We thank Kevan Martin and Johannes Reichold for their valuable comments. We thank Monica Pawelec for English corrections and editing.

This article is freely available online through the *J Neurosci* Open Choice option.

Correspondence should be addressed to Anna Lena Keller, Max Planck Institute for Biological Cybernetics, Spemannstrasse 41, 72076 Tübingen, Germany. E-mail: anna.keller@tuebingen.mpg.de.

DOI:10.1523/JNEUROSCI.2765-10.2011

 0270-6474/11/311246-08$15.00/0

indeed find a difference in vascular density between blob and interblob regions, but one order of magnitude smaller (*Saimiri*, 4.6%; *Macaca*, 4.4%) than published previously. This smaller difference is in accordance with the vascularization and CO activity differences found across cortical layers, which span a considerably larger range.

Materials and Methods

Animals. The brains of two adult squirrel monkeys (*Saimiri sciureus*; one male, 5 years of age; one female, 15 years of age) and two adult macaques (*Macaca nemestrina*; two males, 13 and 15 years of age) were used in this study. The colonies of these animals were bred at the Ludwig Maximilian University of Munich, where they were involved in long-term observations concerning their circadian rhythms and social behavior. No invasive experiments were performed. Animals were killed with pentobarbital (120 mg/kg; in accordance with the guidelines of the American Veterinary Association Panel on Euthanasia and with the recommendations of the National Institutes of Health *Guide for the Care and Use of Laboratory Animals*). All procedures were approved by the local authorities (Regierungspräsidium) and are also in compliance with the guidelines of the European community (EUVD 86/609/EEC) for the care and use of laboratory animals.

Histochemistry. The macaques were perfused transcardially under deep sodium pentobarbital anesthesia with 8 L of 0.9% body temperature heparinized 0.1 M PBS, followed by 2 L of cold 2% paraformaldehyde (PFA) in 0.1 M phosphate buffer (PB), then 4 L of 4% PFA (Roti Histofix; Carl Roth) in 0.1 M PB, and finally 1 L of 10% sucrose (Sigma-Aldrich) in 0.1 M PB. The procedure and the chemicals were the same for the squirrel monkeys, but with only 2 L of 0.9% body temperature heparinized 0.1 M PBS, followed by 0.5 L of cold 2% PFA in 0.1 M PB, then 1 L of 4% PFA in 0.1 M PB, and finally 0.25 L of 10% sucrose in 0.1 M PB. The brain was removed from the skull immediately after perfusion. The primary visual cortex of one hemisphere was removed, slightly flattened with a strip of gauze pressing the piece of tissue with the cortical surface against a glass slide, and postfixed overnight in 4% PFA containing 10% sucrose. The flattening procedure resulted in tangential sections from the lateral surface of the primary visual cortex, approximately parallel to the cortical layers. The other hemisphere was not flattened and was sectioned horizontally. Sections in which the cutting plane was vertical to the cortical surface of V1 were taken for layerwise investigations of CO intensity. The following steps were kept as short as possible to preserve the best obtainable CO activity. For cryoprotection before sectioning, the brain blocks were placed in a series of sucrose solutions of increasing concentration (10, 20, and 30%) in 0.1 M PB until they sank. Sixty-micrometer-thick (previously calibrated) tangential and horizontal sections were then cut on a freezing sliding microtome (Microm HM 440E), for the tangential sections, from the cortical surface to the white matter. All sections were processed first for CO staining (Wong-Riley, 1979, 1989; Wong-Riley and Welt, 1980; Carroll and Wong-Riley, 1984). Incubation times varied between 4 and 8 h, depending on the freshness of the tissue, the time required for cryoprotection, respectively. The sections optimally showing the blobs were afterward processed for fluorescence immunohistochemistry to label collagen type IV to visualize the vasculature (Hamann et al., 1995; Fukuda et al., 2004; Weber et al., 2008). They were collected in 0.1 M PB and then transferred to staining solution consisting of 0.05% DAB (3,3′-diaminobenzidine tetrahydrochloride), 0.04% cytochrome *c* from horse heart, and 3% sucrose (all from Sigma-Aldrich) in 0.1 M PB. Incubation was performed free-floating with gentle agitation at 37°C under visual control until the contrast between blobs and interblobs was found to be sufficient. The staining reaction was stopped by washing three times for 5 min each time in 0.1 M PB. The sections were blocked to prevent nonspecific binding of the antibody by 1 h incubation at room temperature in 10% normal goat serum (collected and provided by the Max Planck Institute for Developmental Biology, Tübingen, Germany), 2% BSA (Sigma-Aldrich), and 0.4% Triton X-100 (Carl Roth). The primary antibody (monoclonal anti-collagen type IV; clone col-94; Sigma-Aldrich) was added to fresh blocking solution (same preparation as above) at a dilution of 1:500 and the sections were incubated for 72 h at 4°C (Zaitsev et al., 2005). They were then washed three times, 5 min, in 0.1 M PBS before being incubated another 72 h at 4°C in the dark in 0.1 M PBS containing a 1:500 dilution of the secondary antibody (Cy-3-conjugated goat anti-mouse IgG (H+L); Jackson ImmunoResearch). After a last series of three washes in 0.1 M PBS, the stained sections were mounted on glass slides and coverslipped wet in polyvinyl alcohol (Mowiol 4–88; Hoechst) containing 4% DABCO (1,4-diazobicyclooctane) (Merck) as an antifading reagent to preserve fluorescence.

Microscopy. Cy-3 and bright-field images of identical fields of view were acquired using a fluorescence microscope (Axiophot; 5× objective; Carl Zeiss) equipped with a monochrome CCD camera (Axiocam MRm, controlled by Axiovision 4.3; Zeiss).

Nomenclature. We followed the naming scheme for layers of the primary visual cortex of Brodmann (1904–1905), with the additional subdivision of layer IVc into two sublayers (namely layer IVc-a and IVc-b) as introduced by Polyak (1957).

Data analysis. Most measurements were made on micrographs taken from the one or two tangential sections through layer II/III that showed the blobs most clearly (see Fig. 1*A*). Twenty two-channel images (see Fig. 2), ~1.1 × 1.4 mm in size, were analyzed per animal. The original Cy3-labeled blood vessel micrographs were filtered, thresholded, and inverted to yield binary images of the vasculature that were appropriate for additional processing (Matlab; The MathWorks) to yield single-pixel-wide midline traces of the vessels (see Fig. 3*A–C*). Larger perpendicular blood vessels were filled manually on the inverted images (see Fig. 3*B*, *B*′) to avoid measuring their circumference instead of their length. The total projected vessel length was measured on these eroded traces; the length density (in millimeters per cubic millimeter) was then stereologically corrected (taking into account the bias induced by the finite section thickness) (Russ and Dehoff, 2000). Details of the density calculation are given in the appendix of Weber et al. (2008). Blobs were identified by visual inspection and region of interest (ROI) borders were manually drawn where staining intensity dropped to background. To test the influence of the manual ROI definition, the ROIs were automatically eroded and dilated in steps of 10% of the original ROI area. For the interblob regions, the total vessel length and volume were determined in the whole image and the sums of the lengths and volumes of the blobs from that respective image were subtracted.

To ensure that the half-automated image processing yielded the same results as a manual delineation of the vasculature (Zheng et al., 1991), two representative images per animal were drawn in Adobe Photoshop CS with a pen tablet (Bamboo Fun; Wacom) on the basis of the anti-collagen staining, further processed as described previously, and the results compared (see Fig. 3*D*). Only minor deviations of these differently generated vessel courses from each other could be observed, and after thorough comparison this effect was rated as negligible. Zheng and colleagues have chosen to define vascular density in millimeters per square millimeter rather than in millimeters per cubic millimeter. It is important to note that the relative difference in percentage between the investigated subregions does not depend on the chosen unit.

For the layerwise evaluation of the CO staining intensity, micrographs from the horizontal sections (like Fig. 1*A*, but monochrome) were taken, and ROIs for the cortical layers and for the blob and interblob regions in lower layer III were defined. For the tangential evaluation, the same CO-stained bright-field micrographs and blob ROIs as described for the blood vessel quantification were taken. The layerwise gray values from the horizontal sections were measured and normalized to make them consistent with the CO activity measurements from previous work (Weber et al., 2008). More precisely, the mean gray value across all layers was normalized to be the same in both studies. The gray values measured on tangential sections that originate only from blob and interblob regions were then normalized to be comparable with the data measured on horizontal sections (mean of blob and interblob from each respective micrograph measured tangentially matched the mean of blob and interblob value measured horizontally).

The evaluation of perpendicular blood vessels was performed on the original Cy3-labeled fluorescent images. They were not defined by their diameter, because some feeding arteries and draining veins already ramify to capillaries in the upper cortical layers (Duvernoy et al., 1981) and could therefore be rather thin when reaching lower layer III, where the

measurements were made. Evaluated vessels ran perpendicularly to the cutting plane and therefore appeared as open (larger vessels) or filled (smaller vessels) circles and were surrounded by the characteristic empty space known as "Zirkumvasaler Kapillarfreier Raum" (Pfeifer, 1930) or "Pfeifer space" as cited by several other authors (Lierse, 1963; Saunders and Bell, 1971; Duvernoy et al., 1981) (see Fig. 2*B*). A boundary box was manually drawn around each perpendicular vessel on the anti-collagen-stained vessel images. Within this boundary box, an ellipse was automatically fitted to the vessel (least-square fit). The minor axis of the ellipse was taken as the estimate of the vessel diameter. An overlay with the blob ROIs provided the definition of blob and interblob vessels. These analyses were performed with Matlab (The MathWorks).

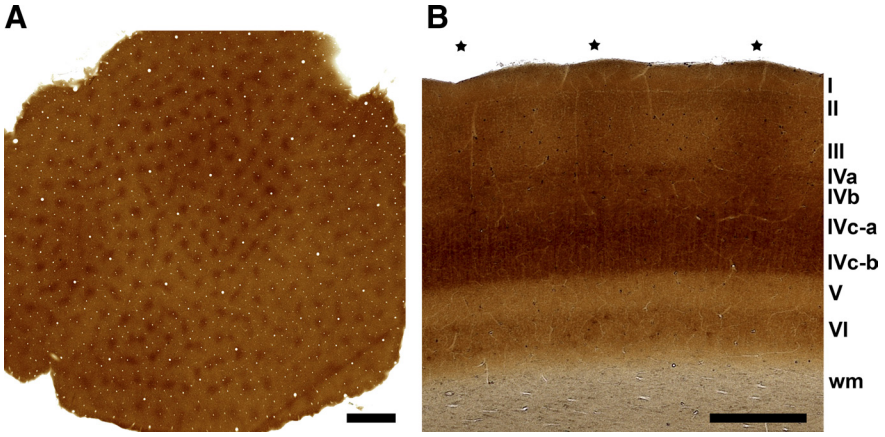

Figure 1. Micrographs of CO staining in tangential and horizontal sections of primate V1; both sections are 60 μm thick and cut frozen on a sliding microtome. ***A***, Low-power magnification overview of a CO-stained tangential squirrel monkey section through layer III of the primary visual cortex, showing the regular distribution and mostly round appearance of the blobs. Scale bar, 1000 μm. ***B***, Micrograph of a CO-stained horizontal macaque monkey section through the primary visual cortex (asterisks denote the positions of the blobs visible in layer III; roman numerals indicate the cortical layers). Scale bar, 500 μm.

Results

Number and distribution of blobs

In both primate species, individual blobs appeared to be mostly round or elliptical in shape and were uniformly distributed in tangential sections through layer III of the primary visual cortex V1 (Figs. 1*A*, 2*A*). On average, a single blob occupied an area of $2.6 \times 10^4 \pm 0.06 \times 10^4$ μm^2 in *Saimiri* and $3.8 \times 10^4 \pm 0.1 \times 10^4$ μm^2 in *Macaca* and occurred with a frequency (see Fig. 4*A*, left-hand side) of $6.8 \pm 0.26/mm^2$ ($\pm$SEM; $n = 406$ blobs in $N = 40$ micrographs) and $7.4 \pm 0.27/mm^2$ ($\pm$SEM; $n = 443$, $N = 40$). Our data revealed no statistically significant difference between the species with respect to the spatial density of blobs, whereas the difference with respect to the mean size of the blobs was significant (independent t test, $t = 9.37$, $p < 0.001$).

Vascular density

The larger blood vessels feeding and draining the capillary bed (i.e., arteries and veins) are running perpendicular to the cortical surface. The number and the mean diameter of these vertical blood vessels was different between squirrel and macaque monkeys (independent t test, $t = -5.42$, $p < 0.001$). We counted 28.2 ± 0.64 vessels/mm^2 in squirrel monkeys ($\pm$SEM; $n = 1675$ vessels in $N = 40$ micrographs) and 23.6 ± 0.57 vessels/mm^2 in macaques ($\pm$SEM; $n = 1407$; $N = 40$) (see Fig. 4*A*, middle). The mean diameter of these vessels was 23.8 ± 0.16 μm in squirrel monkeys and 26.1 ± 0.19 μm in macaques (independent t test, $t = -8.98$, $p < 0.0001$) (see Fig. 4*A*, right). Large perpendicular cortical vessels were preferentially positioned in the interblob regions in both species (see Fig. 4*C*, left-hand side), with 24.9 ± 1.1 vessels/mm^2 in blobs and 28.9 ± 0.7 vessels/mm^2 in interblobs in *Saimiri* and 21.0 ± 1.1 vessels/mm^2 in blobs and 24.7 ± 0.6 vessels/mm^2 in interblobs in *Macaca* ($\pm$SEM; $N = 40$; paired t tests, $t_{Saimiri} = -3.6$, $t_{Macaca} = -3.0$, $p < 0.01$). This corresponded to a ratio of blob to interblob vessels of 1:1.2 in both species if all vertical vessels, of which the smallest had a diameter of 8 μm, were taken into account. However, increasing this threshold changed the ratio (see Fig. 4*E*,*F*). Equal numbers of vertical blood vessels were measured in both areas when only those with a diameter >25 μm (*Saimiri*) or >28 μm (*Macaca*) were counted. By raising the threshold further, the ratio was reversed (slightly higher number of perpendicular vessels within blobs).

Next, we analyzed whether the overall vascular density followed the distribution of the perpendicular vessels. We found that less perpendicular vessels in the blobs correlated with a higher vascular length density. Figure 2 shows an example of a double-stained sample. CO staining was used to define the blobs (Fig. 2*A*) and fluorescent anti-collagen staining to label and quantify the blood vessels (Figs. 2*B*, 3). This analysis showed a generally higher vascular density in the *Saimiri* for all subareas examined (Fig. 4*B*) [i.e., blobs (*Saimiri*, 619.7 ± 12.0 mm/mm^3; *Macaca*, 545.0 ± 8.3 mm/mm^3), interblobs (*Saimiri*, 592.7 ± 10.1 mm/mm^3; *Macaca*, 522.1 ± 9.1 mm/mm^3), and overall (*Saimiri*, 597.1 ± 10.3 mm/mm^3; *Macaca*, 528.4 ± 8.8 mm/mm^3; $\pm$SEM; $N = 40$; independent t tests, $t_{all} \sim -5$, $p < 0.001$)]. Moreover, the vascular length density in the blobs was consistently higher than in the surrounding interblob regions (Fig. 4*D*).

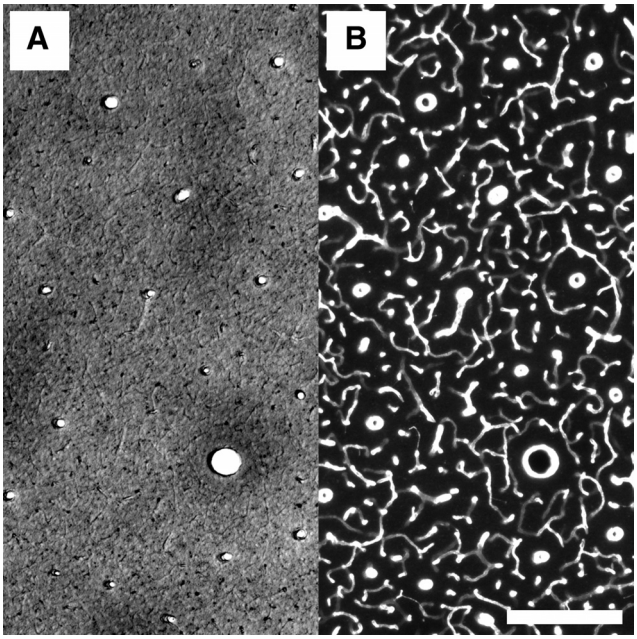

Figure 2. Quality of individual staining for CO activity and blood vessels in double-stained specimen, here a 60-μm-thick tangential section from a squirrel monkey. ***A***, A 50× magnified bright-field micrograph from a similar section as in Figure 1 showing some CO blobs. ***B***, Fluorescence micrograph from the same area of the same section as in Figure 3*A*, showing the blood vessels stained with a primary antibody against collagen type IV and a secondary antibody labeled with Cy3. Scale bar, 200 μm.

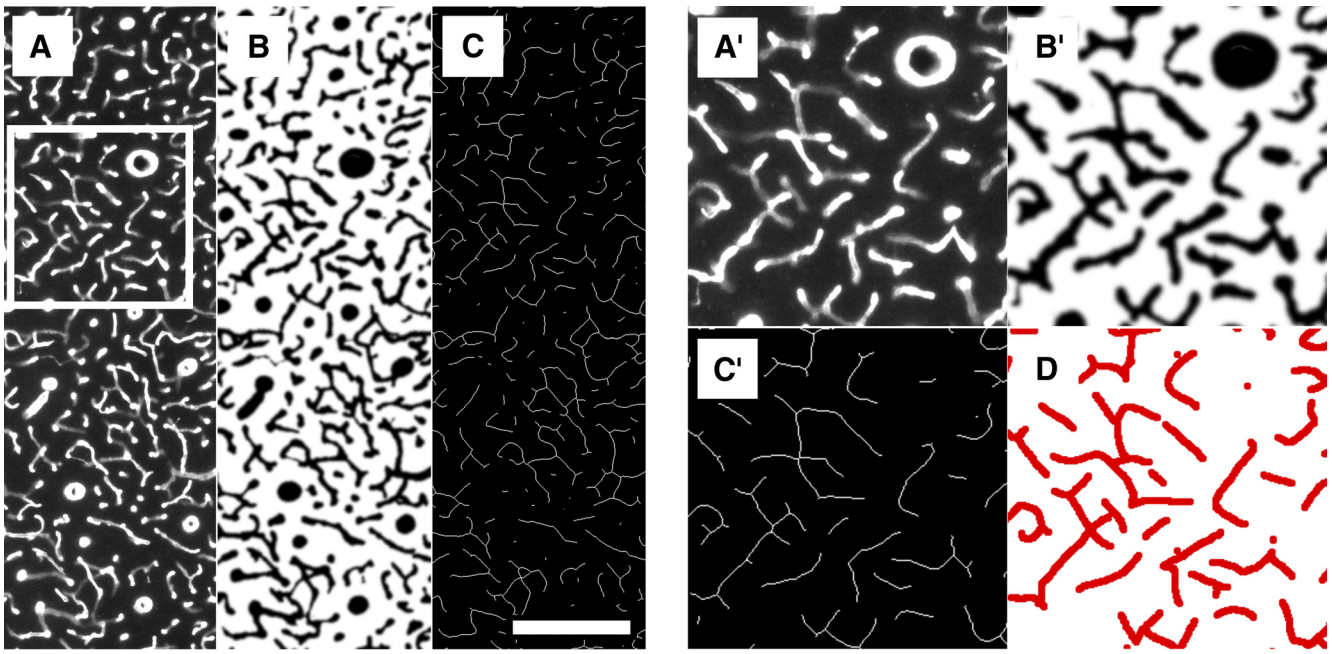

Figure 3. Example of the image-processing protocol of the fluorescent blood vessel images from the same sample as in Figure 2. The anti-collagen immunohistochemistry produced images of high quality that allowed for the semiautomated approach in this study. ***A***, Raw image of an anti-collagen fluorescently stained section. ***B***, The same image as in ***A*** after visually guided semiautomated filtering, thresholding and binarization. ***C***, The same image as in ***B*** after erosion of the vasculature to a line set where the blood vessels are represented by lines of a single pixel width. Scale bar, 200 μm. ***A′***, ***B′***, ***C′***, Enlarged subareas indicated in ***A*** in greater detail in the different image modalities described previously. ***D***, Manual delineation of the raw fluorescent micrograph shows almost no deviation from the course of the eroded lines in ***C′***.

On average, the length density of all blood vessels within blobs was 4.6% higher than in interblob regions in squirrel monkeys and 4.4% higher in blobs compared with interblobs in the macaque ($N = 40$; paired t tests, $t_{Saimiri} = 6.1$ and $t_{Macaca} = 8.3$, $p < 0.0001$). It has to be noted that the measured length density should be unbiased by the unequal distribution of large perpendicular vessels. Whether the measurement of the volume fraction would yield another relationship of blob to interblob vascularization remains an open question. Analysis of the influence of manually identified blob boundaries on the difference in vascular density between blobs and interblobs revealed the existence of a narrow rim surrounding the blobs with an even higher vascular density than within the blobs (*Saimiri*, 624.5 ± 12.4 mm/mm^3; *Macaca*, 554.7 ± 9.6 mm/mm^3). However, this region seems not to belong to the blobs in the strict sense, as no strong CO staining was apparent. When only this rim was compared with the respective interblob area (*Saimiri*, 587.3 ± 10.2 mm/mm^3; *Macaca*, 516.3 ± 9.4 mm/mm^3), the difference was found to be 6.3% for squirrel monkey and 7.4% for macaques ($N = 40$; paired t tests, $t_{Saimiri} = 5.0$ and $t_{Macaca} = 7.9$, $p < 0.0001$). Nevertheless, there were no significant differences between blobs and blob surroundings or between the original and the smaller interblob region.

Cytochrome oxidase activity

The fact that the cytochrome-rich blobs showed a higher microvascular density compared with interblob regions was consistent with the fact that CO activity is a marker for the degree of oxidative metabolism. However, this difference in vascular density was relatively small, particularly when compared with the differences between the cortical layers (Weber et al., 2008). To better understand this discrepancy, we quantified the CO activity in more detail.

The difference in CO staining intensity of blobs compared with interblobs in the horizontal sections was slightly more pronounced in the macaque [Fig. 5*A*, left-hand side: *Saimiri*: 0.05 ± 0.006 arbitrary units (a.u.), $N = 10$; *Macaca*: 0.08 ± 0.010 a.u., $N = 12$; ±SEM; independent t test, $t = 2.53$, $p < 0.05$]. Visual inspection indicated that the difference between blobs and interblob regions was smaller compared with the differences across cortical layers (Fig. 1*A*,*B*). In relative terms, the blob–interblob difference in CO activity was 8% in *Saimiri* and 10% for *Macaca*. This was considerably smaller than the CO activity range across cortical layers, with a respective maximum difference of 64% in *Saimiri* between layer I and the upper subdivision of layer IVc (i.e., layer IVc-a) and 54% in *Macaca* between layer V and layer IVc-a.

Measurements on the tangential sections yielded a more pronounced blob–interblob difference in CO activity in *Saimiri* compared with *Macaca* (Fig. 5*A*, right-hand side: *Saimiri*: 0.07 ± 0.002 a.u., $N = 40$; *Macaca*: 0.06 ± 0.003 a.u., $N = 40$; ±SEM; independent t test, $t = -3.13$, $p < 0.01$).

The overall correlation of CO activity and vascular density in blobs and interblobs was comparable with that observed for the different cortical layers (Fig. 5*C*), despite being measured in sections of different orientations. As a consequence, the regionally different staining intensities, whether between layers or other subareas, reflected differences in vascularization and vice versa (Fig. 5*B*).

Discussion

The energy cost of the brain is the sum of a variety of complex biophysical processes (Attwell and Laughlin, 2001; Jolivet et al., 2009). The local metabolic rate is reflected in regional glucose utilization (Humphrey and Hendrickson, 1983) and, partly, in regional CO activity (Borowsky and Collins, 1989; Wong-Riley, 1989). The proportional consumption of each cerebral element with respect to total brain energy requirements is not clear, and correlating cellular and synaptic density with energy metabolism and vascular density is not straightforward (Baborie and Kus-

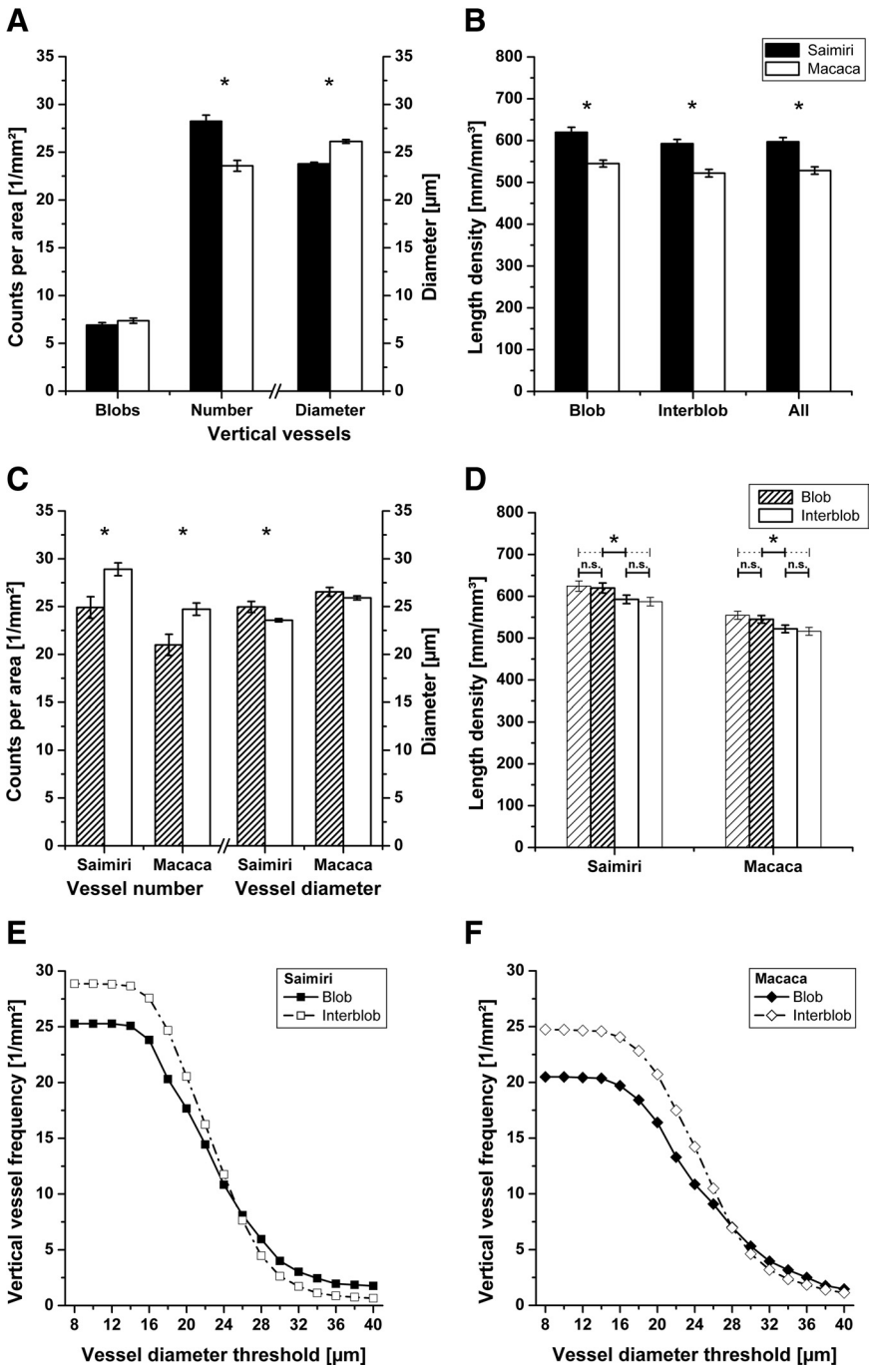

chinsky, 2006; Weber et al., 2008; Tsai et al., 2009). However, metabolic activity is mirrored by regional vascularization (Patel, 1983; Borowsky and Collins, 1989; Weber et al., 2008). The present study is consistent with a strong correlation between oxidative metabolism and vascularization. It is becoming increasingly clear that neuronal activity, cerebral metabolism, and blood flow constitute a tightly coupled ensemble, which is reflected structurally by a vascular density that is highly correlated with local average metabolic activity.

One consequence of this relationship is that brain regions definable anatomically by enzyme histochemistry can be identified *in vivo* using high-resolution hemodynamic imaging. Layer IVc of the macaque's primary visual cortex displays a vascular density that is ~30% higher than in the other layers (Weber et al., 2008). This vascularization difference results in discernability of layer IVc in high-resolution SE BOLD fMRI (Goense et al., 2007). Zheng et al. (1991) have estimated the difference in vascular density between blobs and interblobs in primate V1 to be 42%. Given such a large difference in vascular density, and their relatively large size, blobs should be discernible by state-of-the-art tomographic functional imaging. However, to our knowledge, this has never been shown and the present study now provides the reason for this.

In agreement with Zheng and colleagues, we found a significant difference between blob and interblob regions, but one order of magnitude smaller. Although interindividual variations between the two animals of each species studied here were marginal, it remains possible that other individuals might show more pronounced differences. However, a previous study on layerwise vascularization (Weber et al., 2008) showed very little varia-

Figure 4. Top panel, Interspecies differences in numbers of blobs, numbers and diameters of perpendicular vessels, and density of vascularization. The asterisks indicate a statistically significant difference, and the error bars show SEM. ***A***, The histogram shows counts per area (left *y*-axis) of blobs and vertical blood vessels and mean diameter (right *y*-axis) of vertical blood vessels in squirrel and macaque monkeys. The number of blobs is 8.1% higher in *Macaca* (difference not significant), whereas the number of perpendicular vessels is 19.5% higher in squirrel monkeys compared with macaques. The mean diameter of these vertical vessels is 9.6% greater in macaques. ***B***, The histogram shows the vascular length density in millimeters per cubic millimeter in blobs, interblobs, and overall for the two species investigated. The length density of blood vessels in tangential sections through layer III is significantly different between squirrel and macaque monkeys in all investigated subareas, and the squirrel monkey has in general a ~11.5% higher vascular density than the macaque. Middle panel, Numbers of perpendicular vessels and density of vascularization between blobs and interblobs in primates' V1. The asterisks indicate a statistically significant difference, and the error bars show SEM. ***C***, The histogram shows counts per area (left *y*-axis) and mean diameter (right *y*-axis) of vertical blood vessels in blobs and interblobs of squirrel and macaque monkeys. The left half of the histogram shows the number of perpendicular vessels, and the right-hand side shows the diameters of the vessels in blobs and interblobs. In both species investigated, there are significantly more perpendicular vessels per area in the interblob areas (i.e., 16.1% more in *Saimiri* and 17.6% more in *Macaca*). The diameter of these is only a little larger within the blobs, 5.9% in *Saimiri* and 2.4% in *Macaca*. ***D***, As shown in the histogram, the vascularization of blobs and interblobs is significantly different in both species investigated. The vascular density inside the blobs is 4.6% higher in *Saimiri* and 4.4% higher in *Macaca* compared with the interblob region. The sparsely hatched bar at far left shows vascularization in the immediate surroundings of the blobs, measured in a rim around each blob amounting to 50% of the area of the individual blob. The thinly outlined bar at far right represents vascularization in the interblob region without the surroundings. The vascularization difference between blob surround and respective interblob region is 6.3% in *Saimiri* and 7.4% in *Macaca*. Bottom panel, Cumulative curve showing the number of vertical vessels per area in blobs and interblobs in relation to the threshold diameter applied for the quantification. Note the crossing of the traces at a certain diameter value. Below this threshold there are more perpendicular vessels in the interblob regions, and above it the ratio reverses and more vertical vessels are found within blobs. ***E***, In the squirrel monkey, the threshold diameter is 25 μm. ***F***, In the macaque monkey, the threshold diameter is 28 μm.

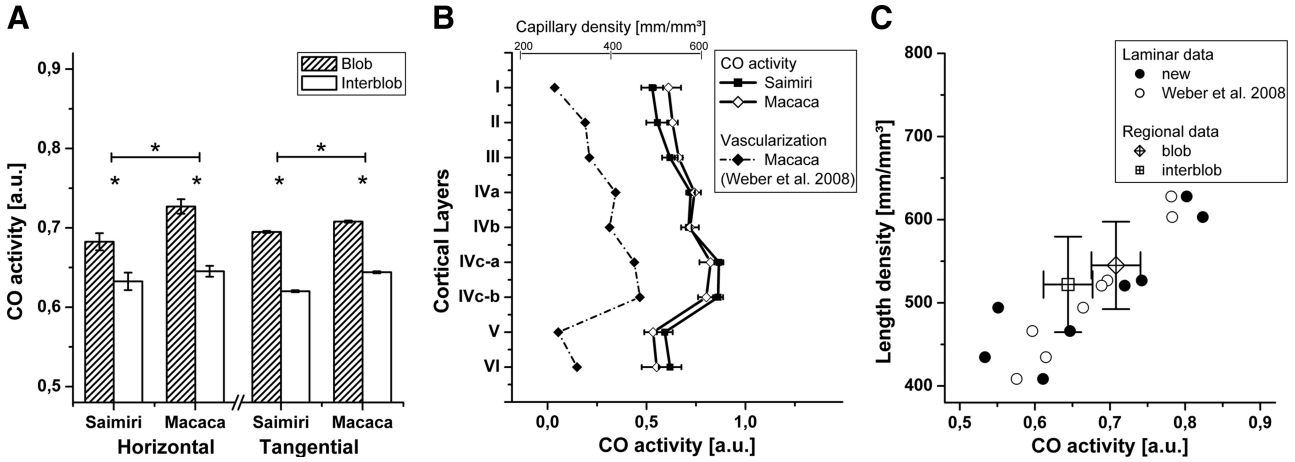

Figure 5. Relative CO activity in blobs and interblobs and across the cortical layers and its correlation to vascular density. Data from Weber et al. (2008) are added. The CO staining intensity was measured as gray values in black-and-white images from vertical sections (as in Fig. 1*B*) and tangential sections (as in Fig. 2*A*). CO activity was normalized as described in Materials and Methods to allow comparison of images from different section orientations, different overall staining intensities, and therefore different image acquisition parameters. The asterisks indicate a statistically significant difference, and the error bars show SEM. ***A***, The histogram shows CO activity in arbitrary units for blobs and interblobs in horizontal and tangential sections from squirrel and macaque monkeys. It is significantly higher in blobs than in interblobs in both species investigated, which is already clearly visible by eye in Figures 1*A* and 2*A*. The differences are comparable across all acquisition modalities. In horizontal sections, it is 7.9% in *Saimiri* and 9.5% in *Macaca*, and in tangential sections, 12.0% in *Saimiri* and 9.9% in *Macaca*. ***B***, The solid traces show the relative CO activity (bottom axis) across all cortical layers of the primary visual cortex in squirrel and macaque monkey. The course of the traces could already be assumed after the visual examination of Figure 1*B*. It also mirrors the capillary density shown in the dashed trace [top axis; only data for the macaque available from the study by Weber et al. (2008)]. ***C***, Correlation between CO activity and vascular density across cortical layers, emphasizing the close relationship between CO activity and vascular length density (filled circles) and the good agreement with previously published data (open circles) (Weber et al., 2008). The data from blob and interblob areas on tangential sections (open squares and diamonds; *x* and *y* error bars show SD) also lie well within the same range.

tion across four animals. Additionally, both CO activity and vascular density measured for blobs and interblobs lie well within the range of the values for the cortical layers (Fig. 5*C*). More specifically, the relative range across cortical layers is similar for CO activity [54%, data from this study; 36% from the study by Weber et al. (2008)] and vascular density [55%, data from the study by Weber et al. (2008)]. The difference in CO activity between blobs and interblobs is considerably smaller (~10%) and accordingly the difference in vascularization can also be expected to be smaller.

The discrepancy between these studies is most likely caused by the different methods used to visualize the blood vessels. Zheng et al. (1991) analyzed CO images to quantify the vascular density. They used transillumination with the condenser aperture stopped down to enhance vessel contrast. It is possible that this might have worked well for the darker CO stained blobs, but not for the unstained interblob region, which could result in underestimation of the vascular density in the interblobs. Our combined fluorescent and bright-field microscopic double-staining approach is unaffected by such bias. The volumetric length density values (in millimeters per cubic millimeter) can easily be converted to the areal length density used by Zheng et al. (1991) (in millimeters per square millimeter). Indeed, we find the absolute numbers for blob regions to be very similar in the two studies, whereas the interblob values of Zheng et al. (1991) are considerably smaller than ours.

Both element density (i.e., sum of neurons, synapses, and glia) and number of incoming connections of the blobs is not as large as that of layer IVc (O'Kusky and Colonnier, 1982; Carroll and Wong-Riley, 1984), although spontaneous activity of blob neurons seems to be comparable with layer IVc (Livingstone and Hubel, 1984). The latter might be related to the lack of orientation selectivity in most blob neurons, which would make them more active in most natural viewing conditions (Livingstone and Hubel, 1984). This could in turn cause the on-average stronger CO staining reactivity of mitochondria in dendrites and axon terminals within blobs, whereas synaptic (Carroll and Wong-Riley, 1984) and cellular densities (Trusk et al., 1990) are not different between blobs and interblobs.

A related more general phenomenon is the coincidence of CO activity with sites of direct thalamic input, as proposed by Wong-Riley (1979), Livingstone and Hubel (1982), Fitzpatrick et al. (1983), and Martin (1988) for review. The blobs receive afferents from the koniocellular layers of the lateral geniculate nucleus, whereas parvocellular and magnocellular layers project to cortical layers IVc and VI (Fitzpatrick et al., 1983; Hendry and Yoshioka, 1994; Ding and Casagrande, 1997). However, it does not seem to be the quantity of synapses alone, but their quality that relates to an increase in CO activity, given the fact that thalamic afferents account for only ~5% of the total amount of excitatory synapses in layer IV in V1 of cats (Ahmed et al., 1994). For layer IVc of V1 of the macaque, a thalamic proportion of ~5–10% of all synapses was reported by Garey and Powell (1971), and Latawiec et al. (2000) estimate that parvocellular afferents build ~8% of all asymmetric synapses there. In V2, thick and pale stripes receive afferents from the same source in V1 (Sincich and Horton, 2002) with the pale stripes in fact getting most of these. However, V2 also receives a major projection from the pulvinar, which matches the distribution of CO activity in V2 (Livingstone and Hubel, 1982; Levitt et al., 1995). Furthermore, Land and Erickson (2005) reported that CO-dark subbarrel domains contain high densities of thalamocortical terminals as shown with a marker for VGluT2 in the rat. In several species, a honeycomb-like pattern was found at the border between neocortical layers I and II, where CO activity and thalamocortical terminations coincide (Ichinohe et al., 2003).

These findings are in accord with the results of Borowsky and Collins (1989): capillary density paralleled glucose utilization and to some extent CO activity; furthermore, the latter coincided spatially with synaptic input from the thalamus. Interestingly, vascular density correlated negatively with lactate dehydrogenase activity. Therefore, different metabolic activity patterns (i.e., the

spatial distribution of oxidative and glycolytic enzymes) might be linked to specific cortical input pathways. The specialized properties of thalamocortical synapses are consistent with this notion. Although the number of thalamic synapses in relation to the excitatory synapses from intracortical sources is small, their impact on the cortical network is significant (Douglas and Martin, 2007). Increased CO activity in thalamic projection sites might arise from the concerted activity of thalamic axon terminals or the postsynaptic properties of their target neurons.

Another noteworthy result of the present study is the different number of perpendicular vessels in blobs and interblobs. Again, there is a discrepancy between previously published data (Zheng et al., 1991) and our own. First, our quantification yielded numbers that are approximately three times higher than in the study by Zheng et al. (1991), and second the local preference of the vertical vessels was the opposite of the previous report (i.e., we found significantly more perpendicular vessels in interblob areas). These discrepancies might arise from the different parameters used for counting. We did not use the diameter of the vessels as a criterion, but their direction with respect to the cortical surface and their morphological characteristics. The vessel caliber was evaluated in a later stage of the analysis. There are different categories of cortical feeding arteries and draining veins defined by their depth of penetration before ramification to capillaries (Duvernoy et al., 1981). The perpendicular orientation of the vessels, clearly visible in tangential sections (Fig. 2*B*), and the characteristic space around these vessels void of capillaries (Pfeifer, 1930; Lierse, 1963; Saunders and Bell, 1971; Duvernoy et al., 1981) were taken as basis for the determination of feeding and draining blood vessels, without taking into account their diameter. It has to be noted that this methodology inevitably underestimates vessel numbers because of the fact that the smallest feeding and draining vessels do not even penetrate layer II/III, from which the tangential sections were taken. However, vessels that already tapered to a small caliber when reaching layer II/III were registered with our approach. This might explain the discrepancy between our data and those published by Zheng et al. (1991), where only perpendicular vessels with a diameter >20 μm were counted. As shown in Figure 4*E*, the threshold set has a great impact on the outcome of the quantification. One possible conclusion is that perpendicular vessels in general (i.e., regardless of their size) are preferentially located between blobs, whereas large perpendicular vessels tend to be located within blobs.

In summary, blobs undoubtedly show a higher metabolic activity, as seen by CO histochemistry, and a small but significantly increased vascular density. This probably reflects the higher metabolic capacity related to the anatomical and functional features of the blob. Unfortunately, the difference in vascular density between blobs and interblobs is small, and the noninvasive neuroimaging techniques of today are unable to detect it.

References

Adams DL, Sincich LC, Horton JC (2007) Complete pattern of ocular dominance columns in human primary visual cortex. J Neurosci 27:10391–10403.

Ahmed B, Anderson JC, Douglas RJ, Martin KA, Nelson JC (1994) Polyneuronal innervation of spiny stellate neurons in cat visual cortex. J Comp Neurol 341:39–49.

Attwell D, Laughlin SB (2001) An energy budget for signaling in the grey matter of the brain. J Cereb Blood Flow Metab 21:1133–1145.

Baborie A, Kuschinsky W (2006) Lack of relationship between cellular density and either capillary density or metabolic rate in different regions of the brain. Neurosci Lett 404:20–22.

Borowsky IW, Collins RC (1989) Metabolic anatomy of brain: a comparison of regional capillary density, glucose metabolism, and enzyme activities. J Comp Neurol 288:401–413.

Brodmann K (1904–1905) Beiträge zur histologischen Lokalisation der Grosshirnrinde—Dritte Mitteilung: Die Rindenfelder der niederen Affen. J Psychol Neurol 4:177–226.

Carroll EW, Wong-Riley MT (1984) Quantitative light and electron microscopic analysis of cytochrome oxidase-rich zones in the striate cortex of the squirrel monkey. J Comp Neurol 222:1–17.

Ding Y, Casagrande VA (1997) The distribution and morphology of LGN K pathway axons within the layers and CO blobs of owl monkey V1. Vis Neurosci 14:691–704.

Douglas RJ, Martin KA (2007) Mapping the matrix: the ways of neocortex. Neuron 56:226–238.

Duvernoy HM, Delon S, Vannson JL (1981) Cortical blood vessels of the human brain. Brain Res Bull 7:519–579.

Fitzpatrick D, Itoh K, Diamond IT (1983) The laminar organization of the lateral geniculate body and the striate cortex in the squirrel monkey (*Saimiri sciureus*). J Neurosci 3:673–702.

Fukuda S, Fini CA, Mabuchi T, Koziol JA, Eggleston LL Jr, del Zoppo GJ (2004) Focal cerebral ischemia induces active proteases that degrade microvascular matrix. Stroke 35:998–1004.

Garey LJ, Powell TP (1971) An experimental study of termination of lateral geniculo-cortical pathway in cat and monkey. Proc R Soc Lond B Biol Sci 179:41–63.

Goense JB, Zappe AC, Logothetis NK (2007) High-resolution fMRI of macaque V1. Magn Reson Imaging 25:740–747.

Hamann GF, Okada Y, Fitridge R, del Zoppo GJ (1995) Microvascular basal lamina antigens disappear during cerebral ischemia and reperfusion. Stroke 26:2120–2126.

Hendrickson AE, Hunt SP, Wu JY (1981) Immunocytochemical localization of glutamic acid decarboxylase in monkey striate cortex. Nature 292:605–607.

Hendry SH, Yoshioka T (1994) A neurochemically distinct 3rd channel in the macaque dorsal lateral geniculate nucleus. Science 264:575–577.

Horton JC, Hedley-Whyte ET (1984) Mapping of cytochrome oxidase patches and ocular dominance columns in human visual cortex. Philos Trans R Soc Lond B Biol Sci 304:255–272.

Horton JC, Hubel DH (1981) Regular patchy distribution of cytochrome oxidase staining in primary visual cortex of macaque monkey. Nature 292:762–764.

Humphrey AL, Hendrickson AE (1983) Background and stimulus-induced patterns of high metabolic activity in the visual cortex (area 17) of the squirrel and macaque monkey. J Neurosci 3:345–358.

Ichinohe N, Fujiyama F, Kaneko T, Rockland KS (2003) Honeycomb-like mosaic at the border of layers 1 and 2 in the cerebral cortex. J Neurosci 23:1372–1382.

Jolivet R, Magistretti PJ, Weber B (2009) Deciphering neuron-glia compartmentalization in cortical energy metabolism. Front Neuroenergetics 1:4.

Land PW, Erickson SL (2005) Subbarrel domains in rat somatosensory (S1) cortex. J Comp Neurol 490:414–426.

Landisman CE, Ts'O DY (2002) Color processing in macaque striate cortex: relationships to ocular dominance, cytochrome oxidase, and orientation. J Neurophysiol 87:3126–3137.

Latawiec D, Martin KA, Meskenaite V (2000) Termination of the geniculocortical projection in the striate cortex of macaque monkey: a quantitative immunoelectron microscopic study. J Comp Neurol 419:306–319.

Levitt JB, Yoshioka T, Lund JS (1995) Connections between the pulvinar complex and cytochrome oxidase-defined compartments in visual area V2 of macaque monkey. Exp Brain Res 104:419–430.

Lierse W (1963) Über Die Beeinflussung der Hirnangioarchitektur Durch Die Morphogenese. Acta Anat 53:1–54.

Livingstone M, Hubel D (1988) Segregation of form, color, movement, and depth: anatomy, physiology, and perception. Science 240:740–749.

Livingstone MS, Hubel DH (1982) Thalamic inputs to cytochrome oxidase-rich regions in monkey visual cortex. Proc Natl Acad Sci U S A 79:6098–6101.

Livingstone MS, Hubel DH (1984) Anatomy and physiology of a color system in the primate visual cortex. J Neurosci 4:309–356.

Lu HD, Roe AW (2008) Functional organization of color domains in V1 and V2 of macaque monkey revealed by optical imaging. Cereb Cortex 18:516–533.

Martin KA (1988) From enzymes to visual perception: a bridge too far? Trends Neurosci 11:380–387.
Murphy KM, Jones DG, Van Sluyters RC (1995) Cytochrome oxidase blobs in cat primary visual cortex. J Neurosci 15:4196–4208.
O'Kusky J, Colonnier M (1982) A laminar analysis of the number of neurons, glia, and synapses in the adult cortex (area 17) of adult macaque monkeys. J Comp Neurol 210:278–290.
Patel U (1983) Non-random distribution of blood vessels in the posterior region of the rat somatosensory cortex. Brain Res 289:65–70.
Pfeifer RA (1930) Grundlegende Untersuchungen für die Angioarchitektonik des menschlichen Gehirns. Berlin: Verlag von Julius Springer.
Polyak S (1957) The vertebrate visual system. Chicago: University of Chicago.
Russ J, Dehoff R (2000) Practical stereology. New York: Plenum.
Saunders RL, Bell MA (1971) X-ray microscopy and histochemistry of human cerebral blood vessels. J Neurosurg 35:128–140.
Sincich LC, Horton JC (2002) Pale cytochrome oxidase stripes in V2 receive the richest projection from macaque striate cortex. J Comp Neurol 447:18–33.
Sincich LC, Horton JC (2005) The circuitry of V1 and V2: integration of color, form, and motion. Annu Rev Neurosci 28:303–326.
Trusk TC, Kaboord WS, Wong-Riley MT (1990) Effects of monocular enucleation, tetrodotoxin, and lid suture on cytochrome oxidase reactivity in supragranular puffs of adult macaque striate cortex. Vis Neurosci 4:185–204.
Tsai PS, Kaufhold JP, Blinder P, Friedman B, Drew PJ, Karten HJ, Lyden PD, Kleinfeld D (2009) Correlations of neuronal and microvascular densities in murine cortex revealed by direct counting and colocalization of nuclei and vessels. J Neurosci 29:14553–14570.
Ts'O DY, Gilbert CD (1988) The organization of chromatic and spatial interactions in the primate striate cortex. J Neurosci 8:1712–1727.
Weber B, Keller AL, Reichold J, Logothetis NK (2008) The microvascular system of the striate and extrastriate visual cortex of the macaque. Cereb Cortex 18:2318–2330.
Wong-Riley M (1979) Changes in the visual system of monocularly sutured or enucleated cats demonstrable with cytochrome oxidase histochemistry. Brain Res 171:11–28.
Wong-Riley MT (1989) Cytochrome oxidase: an endogenous metabolic marker for neuronal activity. Trends Neurosci 12:94–101.
Wong-Riley MT, Welt C (1980) Histochemical changes in cytochrome oxidase of cortical barrels after vibrissal removal in neonatal and adult mice. Proc Natl Acad Sci U S A 77:2333–2337.
Woolsey TA, Rovainen CM (1991) Whisker barrels: a model for direct observation of changes in the cerebral microcirculation with neuronal activity. In: Brain work and mental activity: quantitative studies with radioactive tracers (Lassen NA, Ingvar DH, Raichle ME, Friberg L, eds), pp 189–198. Copenhagen: Munksgaard.
Yoshioka T, Dow BM (1996) Color, orientation and cytochrome oxidase reactivity in areas V1, V2 and V4 of macaque monkey visual cortex. Behav Brain Res 76:71–88.
Zaitsev AV, Gonzalez-Burgos G, Povysheva NV, Kröner S, Lewis DA, Krimer LS (2005) Localization of calcium-binding proteins in physiologically and morphologically characterized interneurons of monkey dorsolateral prefrontal cortex. Cereb Cortex 15:1178–1186.
Zheng D, LaMantia AS, Purves D (1991) Specialized vascularization of the primate visual cortex. J Neurosci 11:2622–2629.